Surface rheology and structure of model triblock copolymers at a liquid-vapor interface: a molecular dynamics study

Article

Accepted Version

Surface rheology and structure of model triblock copolymers at a liquid–vapor interface: a molecular dynamics study

Ahmad Moghimikheirabadi,[*,†] Patrick Ilg,[‡] Leonard M. C. Sagis,[¶] and Martin Kröger[†]

†*Polymer Physics, Department of Materials, ETH Zürich, CH-8093 Zürich, Switzerland*

‡*School of Mathematical, Physical and Computational Sciences, University of Reading, Reading, RG6 6AX, UK*

¶*Food Physics Group, Wageningen University, Bornse Weilanden 9, 6708 WG Wageningen, The Netherlands*

E-mail: ahmadm@mat.ethz.ch

Phone: +41 44 633 6862. Fax: +41 44 632 1076

Abstract

The structure and surface rheology of two model symmetric triblock copolymers with different degree of hydrophobicity but identical polymerization degree, spread at an explicit liquid/vapor interface, are investigated employing extensive equilibrium (MD) and innovative nonequilibrium molecular dynamics (NEMD) simulations with semipermeable barriers (SPB), in both the linear and nonlinear viscoelastic regimes. Results are obtained for interface microstructural and surface rheological quantities under dilatation and surface shear. Our results reveal that the more hydrophilic triblock copolymer ($H_{21}T_8H_{21}$) imparts a higher surface pressure to the interface at a given surface concentration, and takes on a conformation with a larger radius of gyration at the interface, compared with $H_9T_{32}H_9$, where H and T represent chemically different monomers. Increasing the surface concentration and/or decreasing the degree of hydrophobicity leads to an increase of both dilatational storage and loss moduli. Large amplitude oscillatory dilatation (LAOD) tests show that both interfaces exhibit strain softening at high strain amplitudes, while an intracycle nonlinearity analysis reveals an apparent strain hardening in extension. This paradox was already addressed for air-water interfaces stabilized by Pluronics in preceding experimental work. Gyration tensor components parallel and normal to the interface as function of dilatational strain are used to characterize the microstructure; we demonstrate their close relationship to nonlinearity indices in both extension and compression. A structure–rheology relationship is obtained by means of the first harmonic analysis of the surface stress and the corresponding amplitude of the microstructure signal. In-plane oscillatory shear flow simulations are performed as well. The presented approach thus renders possible a test of theoretical frameworks which link interfacial rheological data to the surface microstructure. It is furthermore shown to provide physical insights, which can be used for the interpretation of existing experimental surface rheological data.

Introduction

Complex fluid-fluid interfaces carry adsorbed species that self-assemble into complex (quasi) two-dimensional (2D) microstructures. Such interfaces can be formed by a wide range of surface active

components including proteins, colloidal particles, polymers, lipids, and mixtures of these components.[1] The stability and transient behavior of multiphase systems, emulsions, and foams containing complex interfaces is often dominated by the dynamical properties of the interface.[1] These, in turn, are governed by the fact that the interfacial microstructure is affected by the applied deformation. The interfacial rheology of complex interfaces is therefore typically highly nonlinear.[1–3] Understanding the underlying mechanisms and effect of design parameters is highly relevant for industrial applications, where large processing speeds may probe the nonlinear regime.

Fluid-fluid interfaces can be stabilized by amphiphilic multi-block copolymers. These polymers consist of alternating blocks of hydrophobic and hydrophilic repeating units. One of the key advantages of block copolymers over traditional surfactants is the high level of tailoring that can be done to afford the best stabilization properties.[4–6] Amphiphilic block-copolymers self-assemble into complex 2D microstructures at the interface, including gels, liquid crystals, soft glass phases, micelles, pancake and brush like structures, as revealed by experimental studies.[7–14] Computer simulations further revealed that the type of these microstructures may depend on the surface coverage, chain length, hydrophobic to hydrophilic block ratio, chain stiffness, distribution of blocks, and the degree of hydrophobicity (hydrophilicity) of sub-blocks.[15]

Among different types of multi-block copolymers, special attention has been paid to Pluronics, which are symmetric triblock copolymers of poly(ethylene oxide) and poly(propylene oxide) ($EO_xPO_yEO_x$), and are commercially available in large amounts, with different degrees of hydrophobicity and molecular weights. Motivated by their increasing relevance in fundamental research, industrial applications, pharmaceutical and biomedical areas[16,17], interfacial films of Pluronics have been the subject of numerous experimental studies.[18–29] Surface rheological properties of these films are often measured in the linear regime, and their interfacial microstructures are characterized in (near) equilibrium states, despite the fact that most real life applications involve fast deformation rates and are thus located well within the nonlinear regime. We addressed the former issue recently by performing LAOD tests to interfacial films of Pluronics, and found that they exhibit nonlinearity in their response at relatively large strain amplitudes.[18] The in-situ

characterization of microstructure in the deformed state is extremely difficult as most methods are either applicable to (near) equilibrium systems (e.g. X-ray or neutron scattering techniques), or they require the interface to be transferred to a substrate and hence are destructive to the interface (e.g. atomic force microscopy). Obtaining information about the microstructure at the molecular level in the deformed state is a challenge which can be well tackled by means of computer simulations.

All atomistic MD simulations of Pluronics in bulk – although being limited to extremely small system sizes – have provided us with useful information about their behavior, e.g. their structure and interaction with the cell membrane in aqueous solution.[30] Recent developments of Martini coarse grained (CG) force fields for Pluronics[31] have made it possible to study the equilibrium bulk properties of these systems at larger length scales. While structure, rheology (and their connection) of polymeric bulk systems had been extensively studied in the literature via NEMD simulations on different levels of description[32–36], there have been no studies so far on the interfacial rheology of polymers at molecularly resolved fluid-fluid interfaces. Computer simulations of interfacial films were mostly limited to low molecular weight surfactants and focused mainly on their equilibrium properties such as surface pressure-area isotherms and equilibrium microstructures.[15,37,38] Apart from difficulties in setting up simulations of such heterogeneous systems, applying in-plane affine deformation and decomposing the resulting stress signal into surface and bulk contributions are additional technical difficulties present in simulations of these interfacial systems. The latter is also of major importance in the interpretation of experimental data obtained from interfacial shear rheology experiments.[39,40] There have been a couple of Brownian dynamics simulation[41–43] and theoretical[44] studies on structure and rheology of particle stabilized interfaces in which the bulk phases carrying the interface were treated implicitly via a steep potential well, or not considered at all. While these studies provided physical insights into the surface structure-rheology relationship and allowed making use of classical NEMD algorithms based on homogeneous deformation of the entire simulation box,[45] they neglected (i) the presence of bulk phases that can dramatically alter the interfacial microstructure[46] and (ii) the contribution of momentum transfer between bulk and

interface to the surface stress relaxation, which has recently been shown to be of crucial importance in interfacial dynamics.[15]

Both long-standing deficiencies are overcome in the present work. We simulate the interfacial rheology and structure of Kremer-Grest type[47] FENE multibead-spring model triblock copolymers at a molecularly resolved Lennard-Jones liquid-vapor interface.[15] Employing such CG model we are hence interested in the qualitative structural and dynamical behavior of triblock copolymers, and the effect of block length ratio; the Martini force field has not yet been developed to capture the situation at interfaces quantitatively. A novel method involving 'semipermeable' barriers (SPB) is proposed that can impose in-plane oscillatory deformations to the interface but does not interact with the bulk phase and therefore prevents the occurrence of unphysically strong secondary flows while keeping the number of particles unchanged. Surface rheological data, such as surface storage and loss dilatational moduli are calculated and compared with quantities such as the different components of the gyration tensor, characterizing the interfacial structure. LAOD tests are performed and intracycle nonlinearity measures, strain stiffening and strain rate thickening indices (S- and T-factors),[18,48,49] are calculated and compared with results of recent experiments.[18] Our findings may be of use in the development of constitutive models for the surface stress tensor of block copolymer stabilized interfaces. Such models are required to interpret experimental data obtained from interfacial rheology, taking into account phenomena on the level of the microstructure.

The remainder of this paper is organized as follows. First we introduce the model system and discuss the results of equilibrium MD simulations regarding thermodynamics and surface structure. Afterwards, the NEMD setup is described and validated, and the results of surface dilatational rheology in terms of frequncy- and amplitude sweeps are presented. Nonlinear responses at large strain amplitudes are then quantified by means of Ewoldt's[48] geometrical framework and compared qualitatively against experimental data. Next, a structure–rheology relationship is obtained for the polymeric films studied here by calculating different components of the gyration tensor, and comparing it with the stress signal at different strain amplitudes. Finally, the main results of this study and some lines for future research are outlined in Conclusions. Corresponding results for

sheared surfaces are presented in the Supplementary Information.

Equilibrium MD simulations

In this section, we introduce the simulation setup and present results of extensive equilibrium MD simulations on interfacial microstructure and relaxation times of two kinds of triblock copolymers with different block length ratios.

While there exist different CG models in the literature for block copolymer systems, e.g. models based on the extension of the Matini force field,[31], here we use a Grest-Kremer-type CG model of copolymers in combination with a Lennard-Jones solvent close to its gas–liquid coexistence region that was recently introduced and employed by us in another work.[15] The model system consists of a monoatomic liquid, namely w (water like particle), and a linear multibead-spring symmetric triblock copolymer composed of two types (hydrophilic H and hydrophobic T) of monomers, $\mathrm{H}_n\mathrm{T}_m\mathrm{H}_n$, so that the effect of block length ratio on interfacial properties could be explored systematically upon varying n at a fixed polymerization degree N, while choosing $m = N - 2n$. For the sake of qualitative comparison with the results of our recent experiments,[18] we here study $\mathrm{H}_{21}\mathrm{T}_8\mathrm{H}_{21}$ and $\mathrm{H}_9\mathrm{T}_{32}\mathrm{H}_9$, both carrying $N = 50$ monomers, as their block length ratios are basically identical to the commercially available Pluronic®F-108 and Pluronic®P-123, respectively. Frequency sweeps in our recent experiments on Pluronic F-108 and P-123[18] revealed that their surface rheology is quite similar to that of linear 2D viscoelastic liquids. Therefore, by choosing the degree of polymerization of $N = 50$, it is reasonable to expect that strong entanglements within the interfacial region are avoided and hence this CG model may represent, at least qualitatively, such experimental conditions. All particle (i, j)-pairs (bonded and non-bonded) in the system interact with a Lennard-Jones (LJ) interaction potential with the same size σ but different potential well depths ϵ_{ij} ,

$$V_{ij}(r) = \begin{cases} 4\epsilon_{ij}\left[(\frac{\sigma}{r})^{12} - (\frac{\sigma}{r})^{6}\right] - V_{ij}^{\mathrm{cut}}, & r \leqslant r_{\mathrm{cut}} \\ 0, & r > r_{\mathrm{cut}} \end{cases} \tag{1}$$

Table 1: Lennard-Jones interaction potential well depth ϵ_{ij} among different pairs (i, j) in the system appearing in Eq. 1.

type i	type j	ϵ_{ij} (ϵ)
w	w	1.00
w	H	0.85
w	T	0.40
H	H	0.50
H	T	0.35
T	T	0.40

shifted by $V_{ij}^{\rm cut}$ such that $V_{ij}(r_{\rm cut}) = 0$ at $r_{\rm cut} = 2.5\,\sigma$. Energy parameters ϵ_{ij} are given in Table 1. They are tuned such that $\epsilon_{\rm wH} > (\epsilon_{\rm ww} + \epsilon_{\rm HH})/2$ and $\epsilon_{\rm wT} < (\epsilon_{\rm ww} + \epsilon_{\rm TT})/2$, rendering the middle block hydrophobic and the terminal blocks hydrophilic, and hence the entire molecule surface active. We recently showed via extensive MD simulations[15] that the type of microstructure block copolymers form at the interface, such as homogeneous- or phase segregated interfacial films, is very sensitive on these energy parameters ϵ_{ij}. For Pluronics, experimental evidence points to the formation of (homogeneous) brush-like films (See Ref.[18] and references therein). Therefore the set of ϵ_{ij} energy parameters are selected by performing small-scale exploratory MD simulations of the interfacial system and choosing a set that results in a rather homogeneous stable interfacial film. As shown below, the chosen set is compatible with conditions of weak segregation. $H_{21}T_8H_{21}$ exhibits an approximately 8 times larger hydrophilic/hydrophobic block length ratio than $H_9T_{32}H_9$. To ensure chain connectivity, adjacent beads within the chain interact with an additional finitely extendable nonlinear elastic (FENE) bond potential as

$$V_{\rm FENE}(r) = -\frac{1}{2} k R_0^2 \ln\left[1 - (r/R_0)^2\right], \tag{2}$$

where $k = 30\epsilon/\sigma^2$ is the spring coefficient and $R_0 = 1.5\,\sigma$ is the maximum extension of a bond.[38] The value chosen here for the spring constant k is large enough to avoid bond crossings.[32]

An orthogonal periodic simulation box with dimensions of $L_x = L_y = 50.5\,\sigma$, $L_z = 100.5\,\sigma$,

and a total number of $N_{\text{total}} = 103282$ particles of monomer (H and T) and solvent (w) types are considered, and fixed for all simulations. The open source molecular dynamics package LAMMPS[50] is used to carry out all simulations. Equilibrium MD simulations are performed in the NVT ensemble, and the temperature is fixed at $T = 0.723\,\epsilon/k_{\text{B}}$ by means of the Nosé-Hoover thermostat with a temperature damping time of $0.5\sqrt{m\sigma^2/\epsilon}$. All masses m of particles are considered identical, and an integration time step of $\Delta t = 0.005\sqrt{m\sigma^2/\epsilon}$ is used to integrate Hamilton's equations of motion. The polymer-stabilized liquid-vapor interface is prepared efficiently in three main steps[15,37,38] as follows: (i) A cubic periodic box with dimensions $L_x = L_y = L_{0,z} = 50.5\,\sigma$ is considered which contains N_{total} particles of type w only, and the system is relaxed at the state point of $T = 0.723\,\epsilon/k_{\text{B}}$ and $\rho \approx 0.8\,\sigma^{-3}$ in the liquid phase, close to the liquid–gas coexistence region[51–53] for 10^5 MD steps; (ii) This equilibrated liquid slab is placed in the middle of the final simulation box (with $L_z = 100.5\,\sigma$) and is allowed to reach equilibrium with its vapor phase for another 2×10^5 MD steps, until two liquid-vapor interfaces (because of the periodic boundary condition in the z-direction) are formed parallel to the xy-plane. We note here that the temperature $T = 0.723\epsilon/k_{\text{B}}$ is slightly above the triple point of the LJ fluid[51] and well below its critical temperature $T_c \approx 1.3\epsilon/k_{\text{B}}$ (from Ref.[53]). Thus the entire system should exhibit liquid–gas coexistence at this temperature; (iii) For each polymer molecule to be placed at the interface, the same number of adjacent w particles (each one located at the 1.3σ radial distance neighborhood of the next one) either from the top or the bottom interface are randomly selected and connected together with FENE bonds. Their identity is then changed accordingly to H and T monomers. This procedure is repeated until the desired amount of polymers are placed at both interfaces. Preparing the system in this way ensures the total number density of the system to remain constant at different polymer surface concentrations. The system is then relaxed for 10^6 MD steps and the temperature and different components of the pressure tensor are monitored to ensure that a steady state is reached. Afterwards, a sampling interval of 2×10^6 MD steps is simulated, and a total number of 5000 configurations is stored every 400 MD steps, to calculate ensemble averages and to perform data analysis.

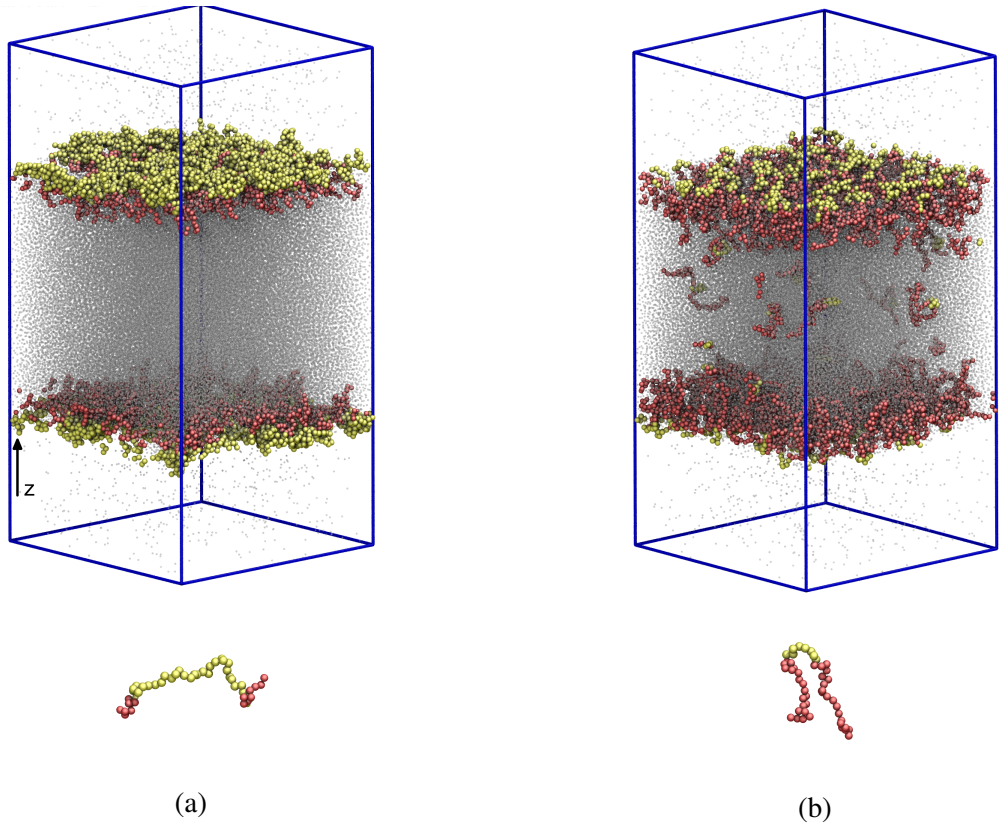

(a) (b)

Figure 1: Equilibrium snapshots of the system containing $2N_p = 170$ triblock-copolymers distributed among the two interfaces for **(a)** $H_9T_{32}H_9$ and **(b)** $H_{21}T_8H_{21}$, resulting in an average surface concentration of $\Gamma = 0.033\,\sigma^{-2}$ and $\Gamma = 0.031\,\sigma^{-2}$ respectively. Representative single chain conformations are shown as well. Gray dots, yellow and red spheres denote w, T and W particles (monomers) respectively. The interfaces are oriented normal to the z-direction.

Equilibrium snapshots of the system containing $2N_p$ triblock copolymers ($N_p = 85$ spread initially at each interface) and their corresponding single chain conformations for $H_9T_{32}H_9$ and $H_{21}T_8H_{21}$ are depicted in Fig. 1a and 1b, respectively. The interfacial polymer films (normal to the z-direction) and liquid and bulk phases are clearly visible in these snapshots. For both copolymer types, the hydrophobic middle block (denoted by yellow spheres) points toward the vapor phase while the hydrophilic terminal blocks (denoted by red spheres) are immersed in the bulk liquid phase. These interfacial films do not seem to show any 2D phase segregation between H and T blocks. This finding is compatible with the value of the Flory-Huggins parameter between H and T monomers defined as $\chi_{\text{H-T}} = \mathcal{Z}\Delta\epsilon_{\text{H-T}}/k_{\text{B}}T$, where $\mathcal{Z}$ is their coordination number and $\Delta\epsilon_{\text{H-T}} = (\epsilon_{\text{H-H}} + \epsilon_{\text{T-T}} - 2\epsilon_{\text{H-T}})/2$. We roughly consider the coordination number to be $\mathcal{Z} \approx 4$

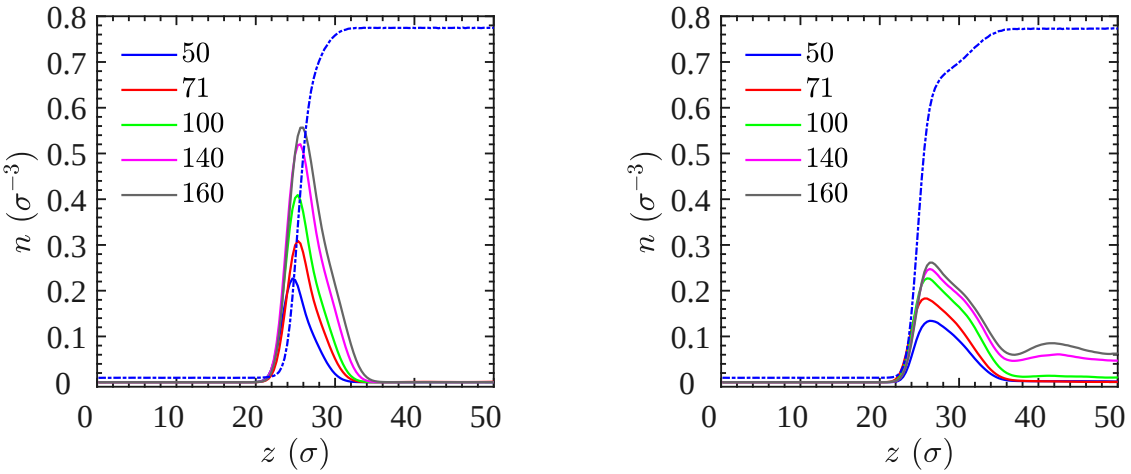

Figure 2: Number density profiles of monomers (solid lines) and solvents (dash-dotted lines) for **(a)** $H_9T_{32}H_9$ and **(b)** $H_{21}T_8H_{21}$ triblock copolymers at one of the two interfaces, the one located at $z \approx 25\sigma$ (surrounded by the gas phase at smaller, and the liquid phase at larger z). Solid lines correspond to different number N_p of polymers initially spread at each interface. Solvent density profiles are evaluated at $N_p = 50$.

–that is the corresponding value for a simple 2D lattice– for our interfacial films. Using the interaction potential parameters given in Table 1 we have $\Delta\epsilon_{\text{H-T}}/k_{\text{B}}T \approx 0.14$, and we arrive at an estimate of $\chi_{\text{H-T}} \approx 0.5$ which within uncertainty of estimate is still in the weak segregation regime ($0 < \chi \leq 0.5$). This value must be considered merely a rough estimate, see e.g. Ref.[54] for a more sophisticated calculation of the χ-parameter via simulation. The snapshots in Figs. 1a and 1b furthermore indicate that the interfacial film of $H_{21}T_8H_{21}$ with larger hydrophilic H moieties is somewhat thicker than that of $H_9T_{32}H_9$, while their degree of polymerization is the same. Despite the fact that both triblock copolymer films are prepared by spreading the same amount of copolymers at the interface, $H_{21}T_8H_{21}$ with relatively larger hydrophilic terminal blocks has a stronger tendency to dissolve into the bulk subphase at the higher surface concentrations (which is energetically more favorable at high surface concentrations) as can be seen in Fig. 1b.

We support these observations by calculating solvent and monomer number density profiles along the z-direction (normal to the interface plane), as shown in Figs. 2a and 2b for systems with different numbers N_p of initially spread $H_9T_{32}H_9$ and $H_{21}T_8H_{21}$ copolymers at each interface. The solvent density profiles, evaluated for $N_p = 50$, clearly indicate that there is a vapor-liquid phase

coexistence in the system with uniform densities in the bulk phases and a rather abrupt change from vapor to the liquid density in the interfacial region. The average bulk density of LJ fluid in the liquid and gas phases are measured as $\rho_l \approx 0.8\,\sigma^{-3}$ and $\rho_g \approx 0.01\,\sigma^{-3}$, around the values reported in the literature[52] for LJ liquid in equilibrium with its vapor phase with a bare liquid–vapor interface. It is noteworthy that the presence of the highly hydrophilic block copolymer $H_{21}T_8H_{21}$ slightly reduces the solvent density in the interfacial region, a phenomenon which we recently pointed out elsewhere.[15,38] The width of the monomer number density profiles reveals that interfacial films of $H_9T_{32}H_9$ are somewhat thinner than those of $H_{21}T_8H_{21}$ triblock copolymers, as $H_{21}T_8H_{21}$ chains are less sharply distributed at the interface and extend toward the bulk liquid phase. Comparing density profiles corresponding to different surface concentrations shows that $H_9T_{32}H_9$, being more hydrophobic, resides at the interface even at relatively high surface coverage while $H_{21}T_8H_{21}$ films begin to dissolve into the subphase, as revealed by nonzero values of densities in the bulk liquid phase. The monomer density profile evaluated at $N_p = 160$ for the $H_{21}T_8H_{21}$ triblock copolymer shows a second peak at $z \approx 42\,\sigma$ in the liquid phase (a distance $\approx 15\sigma$ away from the interface), signaling the formation of a (weak) polymer sublayer, in accordance with the results of Neutron reflectivity measurements[23] which suggested the formation of multilayers for adsorbed layers of Pluronics from concentrated bulk solutions, see supplementary Fig. S7 for individual density profiles of H- and T blocks.

Block copolymers change dramatically the surface (interfacial) tension γ upon adsorption to (or spreading at) the air-water interface. Here we calculate surface tension isotherms $\gamma(\Gamma)$, where $\Gamma = N_{\text{int}}/L_xL_y$ is the surface concentration with $N_{\text{int}} \in [0, N_p]$ being the average number of polymer chains present at the interface. For a periodic simulation box with two planar interfaces oriented normal to the z-direction, surface tension takes the form of[55]

$$\gamma(\Gamma) = \frac{L_z}{2}\left\langle P_{zz} - \frac{1}{2}(P_{xx} + P_{yy})\right\rangle, \tag{3}$$

where P_{zz}, P_{xx} and P_{yy} are diagonal components of the pressure tensor and $\langle ... \rangle$ denotes equi-

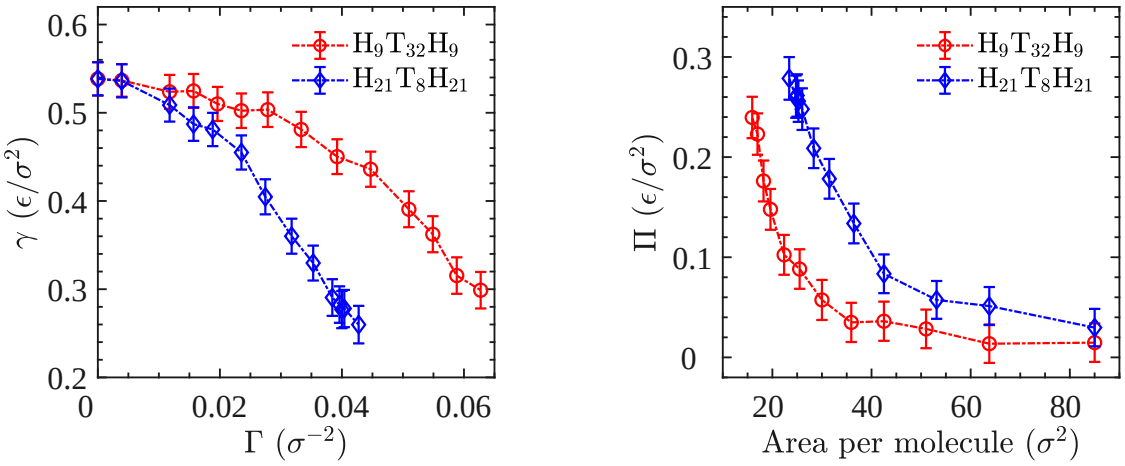

Figure 3: Surface tension as a function of surface concentration **(a)**, and surface pressure-area isotherms **(b)** for $H_{21}T_8H_{21}$ (diamonds) and $H_9T_{32}H_9$ (circles) triblock copolymers. Dashed lines are just a guide for the eyes.

librium ensemble averages. Surface tension isotherms for both systems are presented in Fig. 3a. They indicate that increasing the surface concentration leads to a reduction in the surface tension, which is a typical behavior of surface active agents. However, at a given achievable surface concentration, $H_{21}T_8H_{21}$ forms interfaces with much lower surface tension than $H_9T_{32}H_9$ triblock copolymer, exhibiting a higher surface activity. We note here that increasing the surface concentration of $H_{21}T_8H_{21}$ above $\Gamma \approx 0.04\,\sigma^{-2}$ is extremely difficult, as the interface saturates at this point, and adding more polymers to the interface will make them dissolve into the bulk subphase. This behavior is unlike that of $H_9T_{32}H_9$ surfactants, as they are more hydrophobic and have a higher tendency to stay at the interface, thus leading to a higher surface coverage. In experiments, using a Langmuir trough equipped with a Wilhelmy plate, surface pressure-area isotherms are constructed by plotting the surface pressure $\Pi(\Gamma) = \gamma_0 - \gamma(\Gamma)$ against the average available area per molecule $1/\Gamma$ [18,21], where γ_0 is the surface tension of the bare liquid–vapor interface. Surface pressure-area isotherms for both $H_9T_{32}H_9$ and $H_{21}T_8H_{21}$ triblock copolymers are depicted in Fig. 3b, and indicate that the surface pressure for $H_{21}T_8H_{21}$ is higher, while their overall behavior is the same. A similar trend has been observed in simulations of interfaces stabilized by short amphiphilic surfactants.[38]

On the molecular level, the interfacial microstructure and its variations with surface concentra-

tion can be characterized by the gyration tensor $\mathbf{G}$ of the copolymers, defined by

$$\mathbf{G} = \frac{1}{2N^2} \left\langle \sum_{i,j}^{N} \mathbf{r}_{ij}\mathbf{r}_{ij} \right\rangle, \tag{4}$$

where N is the number of beads with position vectors $\mathbf{r}_i$ within each chain, $\mathbf{r}_{ij} = \mathbf{r}_i - \mathbf{r}_j$, and the average is taken over all chains and the equilibrium ensemble. The mean radius of gyration is then calculated via $R_g = \sqrt{\mathrm{Tr}(\mathbf{G})} = \sqrt{G_{xx} + G_{yy} + G_{zz}}$, where Tr is the trace operator and $G_{\alpha\alpha}$ are diagonal elements of the gyration tensor. Radii of gyration for both triblock copolymers evaluated at different surface concentrations are depicted in Fig. 4a. This figure shows that the more hydrophilic $H_{21}T_8H_{21}$ triblock copolymer takes on a more relaxed conformation with a larger radius of gyration ($\approx$ by 20%) than $H_{21}T_8H_{21}$ over the entire concentration range we examined. Variations of R_g with surface concentration are minor, except at relatively low surface concentrations. In order to gain a deeper understanding of the interfacial microstructural changes, we decompose the gyration tensor into in-plane $\mathbf{G}_{\parallel}$ and normal $\mathbf{G}_{\perp}$ components with the help of the surface projection tensor $\mathbf{P} = \hat{\mathbf{1}} - \hat{\mathbf{k}}\hat{\mathbf{k}}$, defined as $\mathbf{G}_{\parallel} = \mathbf{P} \cdot \mathbf{G} \cdot \mathbf{P}$ and $\mathbf{G}_{\perp} = \mathbf{G} - \mathbf{G}_{\parallel}$, and calculate the corresponding parallel and perpendicular components of the radius of gyration again via the trace, i.e.,

$$R_g^{\parallel} = \sqrt{G_{xx} + G_{yy}}, \qquad R_g^{\perp} = \sqrt{G_{zz}}. \tag{5}$$

Obviously, $R_g^2 = (R_g^{\parallel})^2 + (R_g^{\perp})^2$. These components are shown in Fig. 4b for both triblock copolymers. While R_g remained relatively insensitive to the change of surface concentration, its parallel and normal components with respect to the interface plane change significantly, more specifically $R_g^{\parallel}$ decreases and $R_g^{\perp}$ increases with the surface concentration. In other words, while chains shrink laterally at the interface, they get stretched (normally) toward the bulk subphase. We are going to calculate these microstructural changes in the oscillatory deformed state in a later section and then try to link them with surface dilatational rheology data.

Choosing an appropriate frequency range to perform surface rheology simulations requires knowledge about a characteristic relaxation time of the system. As might be hypothesized from

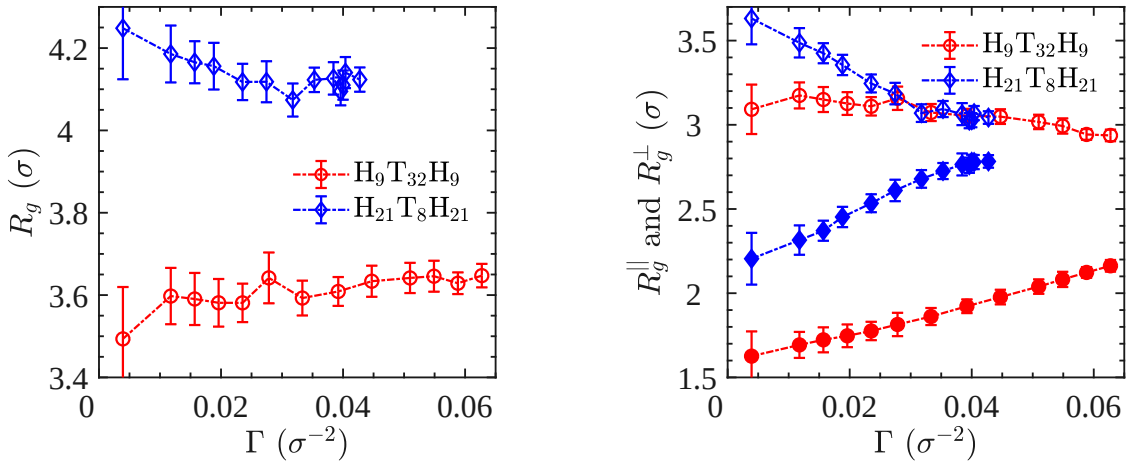

Figure 4: **(a)** Radius of gyration evaluated at different surface concentrations for $H_{21}T_8H_{21}$ (diamonds) and $H_9T_{32}H_9$ (circles). **(b)** Normal (filled symbols) and parallel (open symbols) components of gyration tensor with respect to the interface plane for $H_{21}T_8H_{21}$ (diamonds) and $H_9T_{32}H_9$ (circles).

previous studies of bulk polymeric fluids,[56] the time series for the surface tension shows very fast fluctuations and hence a very short relaxation time (less than one LJ time unit, cf. Supplementary section S1). The more relevant and slower time scale is associated with the relaxation of the chain conformation. To this end, we characterize the dynamics of polymer chains at the liquid-vapor interface by means of the chain end-to-end vector $\mathbf{r}_{\text{ee}} = \mathbf{r}_N - \mathbf{r}_1$ autocorrelation function $C_{\text{ee}}(t)$ defined by

$$C_{\text{ee}}(t) = \frac{\langle \mathbf{r}_{\text{ee}}(0) \cdot \mathbf{r}_{\text{ee}}(t) \rangle}{\langle \mathbf{r}_{\text{ee}}^2 \rangle}, \tag{6}$$

again averaged over all chains. The $C_{\text{ee}}(t)$ results for both triblock copolymers at a surface concentration of $\Gamma = 0.0278\,\sigma^{-2}$ are shown by symbols in Fig. 5a. The simulations show that the relaxation process is slightly slower for $H_{21}T_8H_{21}$ than $H_9T_{32}H_9$ at liquid-vapor interface. Results for $C_{\text{ee}}(t)$ are very well fitted by the Kohlrausch-William-Watts stretched exponential function (as shown by lines in Fig. 5a), which is also suitable to describe the relaxation process in disordered interfacial systems[15], given by

$$C_{\text{ee}}(t) = \exp\left[-(t/\tau_r)^{\beta}\right], \tag{7}$$

where β is the stretch exponent and τ_r is its associated relaxation time. It is then numerically

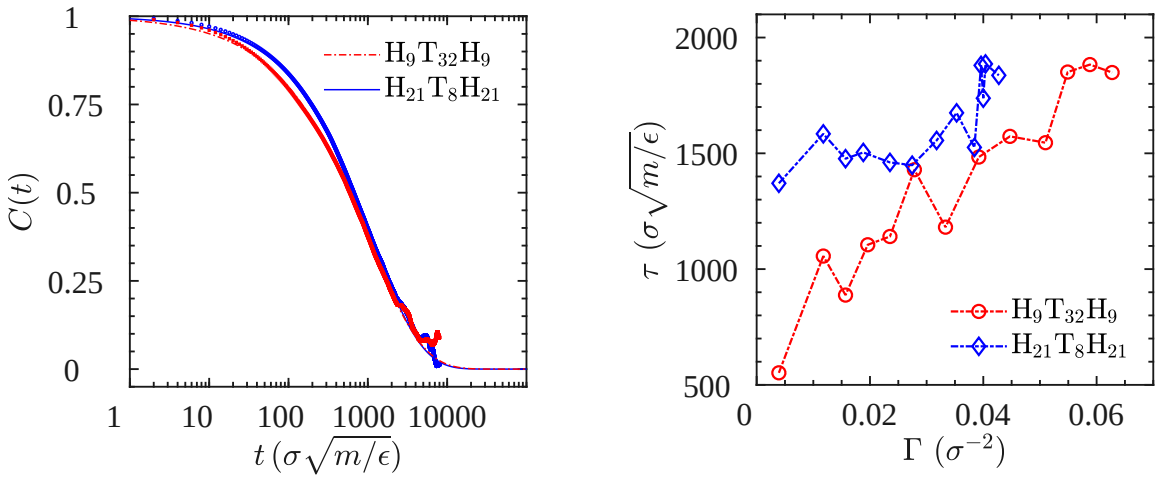

(a) (b)

Figure 5: **(a)** Normalized chain end-to-end vector autocorrelation functions, Eq. (7), for $H_{21}T_8H_{21}$ (blue symbols) and $H_9T_{32}H_9$ (red symbols) and the corresponding fitting of the Kohlrausch-William-Watts (Eq. 7) stretched exponential function (lines) to the simulation data. The stretch exponent β and its associated relaxation time τ_r are calculated as $\beta = 0.65 \pm 0.01$ ($\beta = 0.56 \pm 0.01$) and $\tau_r = 1173 \pm 4\sqrt{m\sigma^2/\epsilon}$ ($\tau_r = 1049 \pm 6$) for $H_{21}T_8H_{21}$ ($H_9T_{32}H_9$) respectively. **(b)** Mean relaxation times τ of $H_{21}T_8H_{21}$ (diamonds) and $H_9T_{32}H_9$ (circles) evaluated from Eq. 8 as a function of surface concentration. The statistical uncertainty of the mean relaxation time, taking into account correlations between snapshots, is $\delta\tau \approx 100\,\sigma\sqrt{m/\epsilon}$.

integrated to obtain the mean relaxation time τ as

$$\tau = \int_0^\infty C_{\text{ee}}(t)dt = \tau_r(\beta^{-1})! \tag{8}$$

where we used factorial notation, i.e., $x!$ is the Gamma function evaluated at $x + 1$. The corresponding mean relaxation times associated with the end-to-end vector autocorrelation at different surface concentrations are shown in Fig. 5b for $H_{21}T_8H_{21}$ (diamonds) and $H_9T_{32}H_9$ (circles) triblock copolymers. It shows that the more hydrophilic triblock copolymer $H_{21}T_8H_{21}$ exhibits a longer relaxation time than $H_9T_{32}H_9$ at the interface, in accordance with the results of our recent experiments.[18] It further indicates that while the relaxation time of $H_9T_{32}H_9$ increases with the surface concentration rather monotonically, for $H_{21}T_8H_{21}$ it remains relatively unchanged until $\Gamma = 0.03\,\sigma^{-2}$, followed by an increase until the interface saturates.

With the information gathered in this section on interfacial microstructure and its relaxation

times at equilibrium, we are ready to perform NEMD simulations on surface dilatational rheology of these films, as will be discussed in the next section.

Surface dilatational rheology

In this section, we introduce and validate a novel simulation setup for NEMD simulations of interfaces using SPB, and afterwards present dilatational rheology results of amplitude and frequency sweeps obtained with the help of this method.

Simulation using semipermeable barriers

Most NEMD simulation algorithms are based on homogeneous deformation of the entire simulation box,[45] and hence not applicable to the field of surface rheology. In this context one needs to apply an in-plane deformation only to the interfacial film and not to the bulk phases, and then measure the corresponding interfacial stresses as a result of deformation. In the experiments, Langmuir troughs with movable barriers have been widely used to apply in-plane oscillatory dilatational deformations to films spread at the air-water interface.[18–20,26] Inspired by these surface rheology experiments, we use the simulation setup described in the previous section and introduce two unstructured, repulsive semipermeable barriers (SPBs) at each of the sides of the interfacial film, oriented normal to the x-direction. Figure 6 shows a simulation snapshot including these SPBs. They resemble "movable barriers" in the Langmuir trough setup. To reduce secondary effects due to unwanted deformation of the bulk liquid, these SPBs are "ideal" in the sense that they only exert in-plane repulsive forces (in the x-direction) to the interfacial film, i.e., no shear force, and are permeable to the solvent (w) particles, so that when they move they only deform the interface laterally in the first place. Only H and T segments interact with the purely repulsive SPBs as long as they are sufficiently close to it. More precisely, a segment at normal distance $\Delta x = |x - x_{\text{SPB}}|$ from a SPB at x_{SPB} experiences a purely repulsive LJ potential with a depth of ϵ, i.e., $V_{\text{SPB}}(\Delta x) = 4\epsilon[(\sigma/\Delta x)^{12} - (\sigma/\Delta x)^{6} + 1/4]$ for $\Delta x \leq 2^{1/6}\,\sigma$, and $V_{\text{SPB}}(\Delta x) = 0$ otherwise,

while solvent particles remain subject to periodic boundary conditions in all directions.

The oscillatory dilatational strain is applied to the interface through oscillating the SPBs symmetrically in the x-direction back and forth with an amplitude l_0 and angular frequency of $\omega = 2\pi f$ about the initial distance between the barriers, L_0 (6). The SPB positions are thus given by $x_{\text{SPB}}(t) = \pm[L_0/2 - l_0 \sin(\omega t)]$ such that the confined area between the two SPBs (interfacial area) is subjected to the following variation

$$A(t) = A_0 + \Delta A \sin(\omega t), \qquad \Delta A = 2 l_0 L_y, \tag{9}$$

where $A_0 = L_0 L_y$ is the initially undeformed area of the polymer-vapor interface. The corresponding dilatational strain $\epsilon_d(t)$ is

$$\epsilon_d(t) = \frac{A(t) - A_0}{A_0} = \frac{\Delta A}{A_0} \sin(\omega t). \tag{10}$$

and the transient surface pressure is directly evaluated at each of the SPBs through

$$\Pi(t) = \langle F_{\text{SPB}}(t) \rangle / L_y, \tag{11}$$

where F_{SPB} is the normal force exerted on the SPB, and $\Pi(t)$ short notation for $\Pi(\Gamma(t))$. The surface extra dilatational stress $\sigma_d(t)$ is calculated from $\sigma_d(t) = \Pi_0 - \Pi(t)$, where $\Pi_0 = \langle F_{\text{SPB}}/L_y \rangle$ is the mean value of the surface pressure signal. With $\epsilon_d(t)$ and $\sigma_d(t)$ at hand, the surface complex dilatational modulus E^* is calculated via

$$E^*(i\omega) = E'(\omega) + iE''(\omega) = \frac{\mathcal{F}\{\Pi_0 - \Pi(t)\}}{\mathcal{F}\{(A(t) - A_0)/A_0\}} = \frac{\mathcal{F}\{\sigma_d(t)\}}{\mathcal{F}\{\epsilon_d(t)\}}, \tag{12}$$

where E', E'' are the dilatational storage and loss moduli respectively, and $\mathcal{F}$ is the Fourier transform operator. In the linear regime, where the strain amplitude $\Delta A/A_0$ is small enough, E^* is independent of strain amplitude and the response consists of only a single harmonic with the same

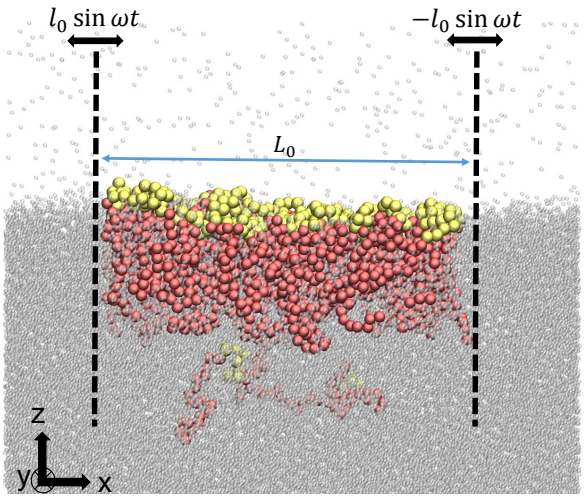

Figure 6: The SPB method. Simulation snapshot of $H_{21}T_8H_{21}$ projected to the x-z plane at the liquid-vapor interface subject to oscillatory dilatation in x-direction about initial distance $L_0 < L_x$. Red and yellow spheres stand for H and T segments respectively, while gray dots represent w particles. Semipermeable two-dimensional barriers (black dashed lines) are oriented normal to the x-direction and oscillate in the opposite directions with the same amplitude and frequency, thus creating an oscillatory in-plane dilatational field.

frequency ω as the deformation, and can be written in the following form

$$\sigma_d(t) = \Delta\Pi \sin(\omega t + \delta), \tag{13}$$

where $\Delta\Pi$ denotes the amplitude of the signal and $\delta \in [0, \pi/2]$ is the phase shift of the response with respect to the deformation. Inserting Eqs. 10 and 13 into Eq. 12, the surface dilatational moduli are obtained as

$$E'(\omega) = \frac{\Delta\Pi}{\Delta A/A_0} \cos(\delta), \quad E''(\omega) = \frac{\Delta\Pi}{\Delta A/A_0} \sin(\delta). \tag{14}$$

The simulation setup introduced here is very much similar to the Langmuir trough experiments with symmetric barriers, and as a result the deformation field applied to the interface (Eq. 9) is uniaxial and not purely dilatational. Hence, the moduli we present here are Young and not dilatational moduli. We do not distinguish between the two quantities because the interfacial films do not show surface elasticity in shear, and therefore surface Young and dilatational moduli are equal.[1] For the

corresponding study of sheared interfaces, of minor relevance for the present model system, but fully discussed in the Supplementary Information section S5, we use semipermeable, structured barriers (SPSB).

Validation of the semipermeable barrier approach

After preparing and relaxing the interfacial system including the SPBs with the procedure just described, dynamic simulations are performed in the canonical NVT ensemble. We employ a stochastic Langevin thermostat in the neutral y- direction with a damping time of $0.05\sqrt{m\sigma^2/\epsilon}$ to control the temperature at $T = 0.723\,\epsilon/k_{\mathrm{B}}$ while leaving the x- and z-components of all velocities unconstrained. The damping time is chosen small enough to ensure that the overall profile-unbiased temperature remains constant within thermal fluctuations. A total number of 70 oscillation cycles per simulation were carried out, and the last 50 cycles were used to evaluate time averages.

To validate the approach we calculated the in-plane velocity profiles of the interfacial film imposed by these SPBs. To obtain a large signal/noise ratio, we measured the local in-plane velocity profiles $v_x(x)$ at maximum deformation rate, corresponding to $t = 2k\pi/\omega$, where k is an integer and $\omega = 2\pi f$ is the angular frequency of the SPB oscillation. The in-plane velocity profiles of the interfacial film of $H_{21}T_8H_{21}$ at a surface concentration of $\Gamma = 0.0384\,\sigma^{-2}$ for selected dilatational strain amplitudes of $\Delta A/A_0 = 0.04$, 0.06, 0.08 and 0.10 are indicated in Supplementary Fig. S2. The results clearly show that a linear velocity profile slightly away from the wall is achievable using these SPBs at relatively small strain amplitudes $\Delta A/A_0 \leq 0.08$.

For larger amplitudes there exists a nonlinear velocity profile accompanied by an apparent normal velocity slip at the SPBs whose strength is affected by the mechanical properties of the interfacial film, deformation amplitude (rate), and the sample-SPB interaction potential V_{SPB}. The crossover amplitude is confirmed, while less directly, by macroscopic properties presented in the following sections. For a perfectly elastic film the deformation propagates affinely through the sample while for an ideal viscous interface the center of the film might not even feel the motion of the barriers due to viscous dissipation, and the deformation becomes non-affine. It is interesting to

see that for a viscoelastic interface – of the triblock copolymers studied here – a mixed behavior in the deformation is observed over the range of parameters explored. Quantitative modeling of real substances via an appropriate V_{SPB} thus requires knowledge about the velocity profile as an indicator for the microscopic interactions at the liquid-barrier interface. Such nonlinearities are usually not considered in the interpretation of Langmuir trough data, while bulk properties far from the interface may be mainly determined by the bulk flow gradients. The nonlinearities during dilatation should occur in real samples depending on the system specifications and do not falsify the method itself. For the sake of comparison with the experimental results, we report all the interfacial properties as a function of imposed deformations, while the simulations would allow to present results versus the actual deformation rates measured in the center of the interface. Relationships between stress and conformation, as discussed later below, are not affected by this choice.

We have furthermore validated the approach for the case of in-plane shear flow. Here, structured, semipermeable, and partially attractive walls are considered to couple the barrier to the polymers. The shear velocity profile is linear, and there is no sign of wall slip for the interaction potential considered, cf. Supplementary Fig. S5.

Surface rheological results

To investigate interfacial dynamics via surface dilatational rheology simulations, frequency sweeps in the linear regime have to be performed. To this end, one needs to find strain amplitudes that are small enough so that the system response is still in the linear regime and large enough so that the noise to signal ratio is sufficiently small. Therefore, strain amplitude sweeps should be performed first. For amplitude sweeps, an oscillatory deformation time period $\tau_{\mathrm{flow}} = 2\pi/\omega_{\mathrm{flow}} = 200\sqrt{m\sigma^2/\epsilon}$ is chosen such that the Deborah number using an approximate relaxation time of $\tau = 1500\sqrt{m\sigma^2/\epsilon}$ (obtained from Fig. 5b) is $\mathrm{De} = \tau/\tau_{\mathrm{flow}} \approx 7.5$, and hence the interfacial response is in the viscoelastic domain. It is noteworthy that a deformation with $\mathrm{De} \ll 1$ captures purely viscous and $\mathrm{De} \gg 1$ purely elastic behavior of the interface[57]. Amplitude sweep results for E^* of $\mathrm{H_{21}T_8H_{21}}$ evaluated at two different surface concentrations are presented in Fig. 7a. In-

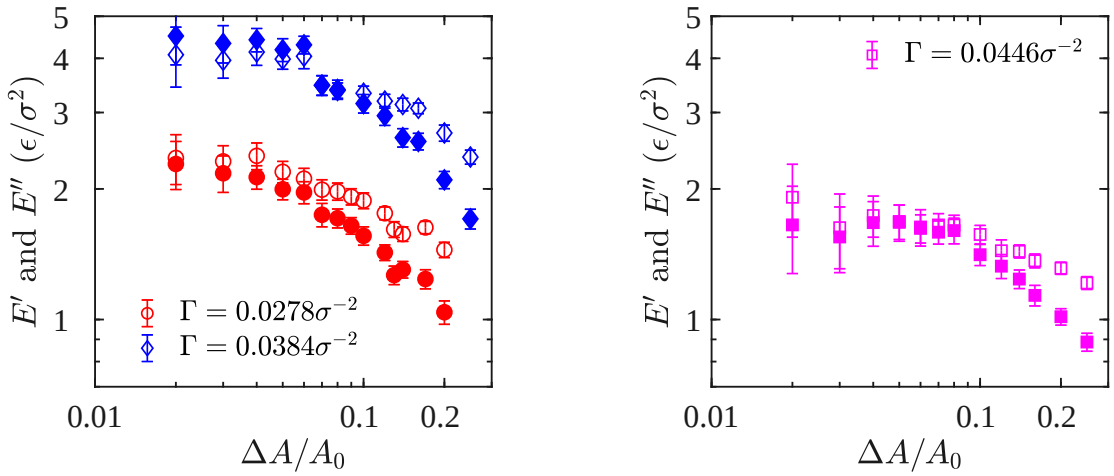

Figure 7: Amplitude sweeps to pick up the right strain amplitudes in the linear regime. Dilatational loss E'' (close symbols) and storage E' (open symbols) moduli for **(a)** $H_{21}T_8H_{21}$ measured at two different surface concentrations, and **(b)** $H_9T_{32}H_9$ interfacial films evaluated at different oscillatory strain amplitudes at a fixed frequency of $f = 0.005\sqrt{\epsilon/m\sigma^2}$ for both triblock copolymers.

creasing the surface concentration from $\Gamma = 0.0278\,\sigma^{-2}$ to $\Gamma = 0.0384\,\sigma^{-2}$ (close to the saturation concentration) approximately doubles both moduli. Furthermore, a linear regime for both surface concentrations up to $\Delta A/A_0 \approx 0.05$ is observed, in agreement with our expectations from the velocity profile measurements. For strain amplitudes beyond this, the macroscopic response enters the nonlinear regime and the interface indicates strain softening for both surface concentrations. Interfacial films of $H_9T_{32}H_9$ also show a similar behavior, as depicted in Fig. 7b. However, these films have lower moduli and a linear domain which extends to a larger strain amplitude of $\Delta A/A_0 \approx 0.09$. Strain softening at large strain amplitudes has been observed experimentally for numerous materials such as proteins and colloidal particles at fluid-fluid interfaces, see e.g. Ref.[49] and references therein. A quantitative description of intracycle nonlinearities at large strain amplitudes is given in the next section.

Frequency sweeps are performed with a strain amplitude of $\Delta A/A_0 = 0.04$, resulting in a response in the linear regime as revealed by amplitude sweep tests. The results for $H_{21}T_8H_{21}$, evaluated at two different surface concentrations, and $H_9T_{32}H_9$ triblock copolymer interfacial films are presented in Figs. 8a and 8b, respectively. We observe that $H_9T_{32}H_9$ (being more hydrophobic

than $H_{21}T_8H_{21}$) has lower moduli compared to $H_{21}T_8H_{21}$, over the entire frequency range, even though its surface concentration is higher, a behavior that has been observed also experimentally in Ref.[18] for interfacial films of Pluronics. Both E' and E'' indicate a power law behavior at small frequency domain (up to $0.01\sqrt{\epsilon/m\sigma^2}$) which is then followed by a plateau in the loss modulus and a weak increase in the elastic modulus with frequency. This region (in the frequency range of 0.01–1.0 $\sqrt{\epsilon/m\sigma^2}$) is similar to the rubbery (elastic) region of polymer melts where the response is elastic dominant and the dynamic modulus is relatively insensitive to frequency.[57] Therefore, the overall behavior for both triblock copolymers confined to an interface resembles similarities to that of entangled bulk polymeric liquids with different scaling exponents in the frequency domain below the plateau region. A similar qualitative comparison has been made for shear viscoelasticity of end-tethered polymer monolayers at the air-water interface in Ref.[58]. While E'' seems to scale with a slightly larger exponent than E', both exponents are still identical within errors; both approximately scale with frequency as E', $E'' \propto f^{0.5}$ over the f range investigated, see Table 2 for the exact values including statistical errors. This scaling is unlike that of linear viscoelastic liquids where $E' \propto f^2$ and $E'' \propto f$ in the small frequency domain. It is in fact equal to that of the Lucassen van den Tempel model,[59] but on the timescales that the simulations are performed, there is no exchange of polymers between bulk and interface and therefore this model cannot be tested or applied here. It clearly shows that constitutive models based on direct generalization of three-dimensional bulk rheology will fail to interpret surface rheology data here, and models which take into account the coupling of the interface to their bulk phases[15] and interfacial microstructure in a thermodynamically consistent manner[1] are needed to be developed for interfacial rheology.

Lissajous plots, LAOD

In this section we present and discuss the raw oscillatory signals by means of Lissajous plots and quantify intracycle nonlinearities in the LAOD tests. When an interface is deformed with a relatively large strain amplitude at a given frequency, higher harmonics may appear in the response as

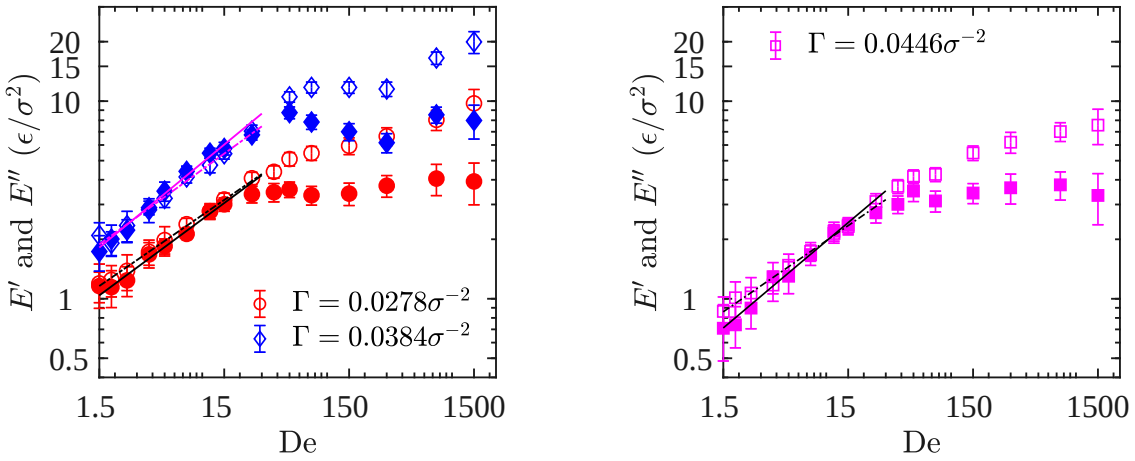

Figure 8: Frequency sweeps with a dilatational strain amplitude of $\Delta A/A_0 = 0.04$. The horizontal axis shows the Deborah number $\mathrm{De} = f\tau$ with a mean relaxation time of $\tau \approx 1500\sqrt{m\sigma^2/\epsilon}$. Dilatational modules E' (open symbols) and E'' (close symbols)for $H_{21}T_8H_{21}$ **(a)**, measured at two different surface concentrations, and $H_9T_{32}H_9$ **(b)** triblock copolymer interfacial films. Included are power law fits $E' \propto f^a$ (dash-dotted lines) and $E'' \propto f^b$ (solid lines) in the small frequency region.

a result of structural changes induced by the large deformation. More specifically, higher *odd* harmonics may emerge in the response to shear deformation, due to the insensitivity of materials with respect to the direction of the shear, and both odd and even harmonics may appear in the response to dilatational deformation, as materials tend to have asymmetric response in extension compared to compression. The dynamic moduli as presented in Fig. 7b, are by definition (Eq. 12) related to the first harmonic of the stress signal, and hence for the nonlinear regime, where higher harmonics may appear in the response, are not a full descriptor of the material response. Therefore, one needs to look at the raw signal to gain a better understanding of the material response as a result of large

Table 2: Power law exponents for the scaling of $E' \propto f^a$ and $E'' \propto f^b$ in the small frequency domain calculated from a nonlinear least squares fitting of the simulation data presented in Fig. 8.

Block copolymer	$\Gamma(\sigma^{-2})$	a	b
$H_{21}T_8H_{21}$	0.0278	0.43 ± 0.04	0.47 ± 0.04
$H_{21}T_8H_{21}$	0.0384	0.46 ± 0.05	0.52 ± 0.06
$H_9T_{32}H_9$	0.0446	0.44 ± 0.04	0.53 ± 0.07

deformations. To this end, we present the raw signal by means of an elastic Lissajous plot, where the surface stress $\Pi_0 - \Pi(t)$ is plotted against dilatational strain $(A(t) - A_0)/A_0$ in a cyclic loop. A linear viscoelastic response is manifested as a tilted ellipse, and nonlinearities in the response lead to a distortion in the shape of these curves. Lissajous plots for $H_{21}T_8H_{21}$ at $\Gamma = 0.0384\,\sigma^{-2}$ and $H_9T_{32}H_9$ at $\Gamma = 0.0446\,\sigma^{-2}$ corresponding to the amplitude sweeps shown in Fig. 7 measured at a constant frequency of $0.005\sqrt{\epsilon/m\sigma^2}$ are depicted in Fig. 9a and 9b respectively. It clearly indicates that while for relatively small strain amplitudes the overall signal remains in the linear viscoelastic regime (as revealed by an elliptic shape), increasing the deformation amplitude results in a Lissajous curve which becomes progressively more distorted, an indication for a stronger nonlinearity in the response. While emergence of higher odd harmonics in LAOS tests preserves the symmetry of the Lissajous curves, the signal in LAOD contains both even and odd harmonics, which is manifested by asymmetry of the response in extension (the upper half of the curves) compared with the compression (the lower half of the curves). Furthermore, for both triblock copolymers, a widening of the Lissajous curves is observed with increasing strain amplitude, which indicates that the viscous contribution to the stress signal becomes more dominant due to the possible in-plane structural changes. A semi-plateau in the response at the end of the extension part of the cycle is observed, implying that the interfacial structure has yielded, and the subsequent response is strain softening in extension, consistent with the result of the amplitude sweeps shown in Fig. 7.

While Lissajous plots provide valuable qualitative information regarding nonlinearities in the response to deformation, we further quantify these plots by employing the geometrical framework developed by Ewoldt et al.[48], and later was slightly modified to be applicable to dilatational rheology data.[18,49] In order to describe elastic nonlinearities, four geometrically motivated intracycle dynamic dilatational moduli are defined: minimum- and large-strain dilatational moduli in extension (E'_{EM}, E'_{EL}), and in compression (E'_{CM}, E'_{CL}), see Fig. 10a. Likewise, in a viscous Lissajous plot where the surface stress is plotted against the strain rate, four intracycle dynamic dilatational viscosities can be defined: minimum- and large-rate daynamic dilatational viscosities in extension($\eta'_{d,\mathrm{EM}}$, $\eta'_{d,\mathrm{EL}}$), and in compression ($\eta'_{d,\mathrm{CM}}$, $\eta'_{d,\mathrm{CL}}$) which are all depicted in Fig. 10b.

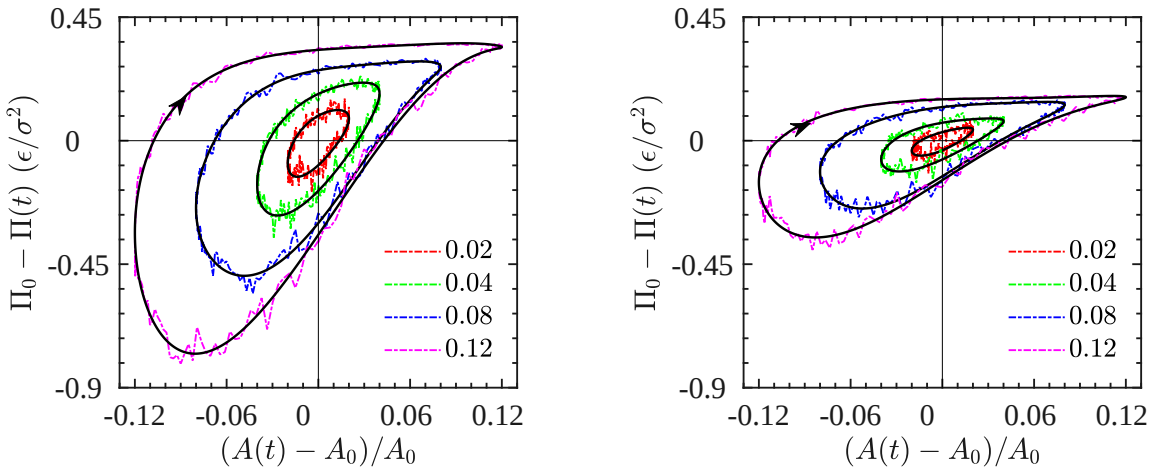

Figure 9: Lissajous plots (dash-dotted curves) corresponding to the LOAD data shown in Fig. 7 for interfacial films of $H_{21}T_8H_{21}$ at $\Gamma = 0.0384\sigma^{-2}$ **(a)**, and $H_9T_{32}H_9$ at $\Gamma = 0.0446\sigma^{-2}$ **(b)**. Solid curves indicate processed signals containing only the first four harmonics of the raw dilatational stress.

With these intracycle moduli and viscosities at hand, the strain-stiffening and strain rate-thickening indices in extension $S_{\rm E}$, $T_{\rm E}$ and compression $S_{\rm C}$, $T_{\rm C}$ are then calculated as[49]

$$S_{\rm E} = \frac{E'_{\rm EL} - E'_{\rm EM}}{E'_{\rm EL}}, \qquad S_{\rm C} = \frac{E'_{\rm CL} - E'_{\rm CM}}{E'_{\rm CL}}, \tag{15}$$

and[18]

$$T_{\rm E} = \frac{\eta\prime_{d,\rm EL} - \eta'_{d,\rm EM}}{\eta'_{d,\rm EL}}, \qquad T_{\rm C} = \frac{\eta'_{d,\rm CL} - \eta'_{d,\rm CM}}{\eta'_{d,\rm CL}}, \tag{16}$$

where $S = 0$ for a linear elastic response, $T = 0$ for a linear viscous response, $S < 0$ ($S > 0$) indicates strain-softening (strain-hardening) and $T < 0$ ($T > 0$) shows strain-rate thinning (strain-rate thickening) in extension $_{\rm E}$ or compression $_{\rm C}$. The strain-stiffening indices as a function of dilatational strain are presented in Fig. 11a for interfacial films of $H_{21}T_8H_{21}$ and $H_9T_{32}H_9$ triblock copolymers. It shows that for relatively small strain amplitudes the elastic response is linear $S \approx 0$, and for increasing amplitude that the nonlinearity both in extension $S_{\rm E}$ and compression $S_{\rm C}$ becomes progressively more pronounced, due to the microstructure variations at these strain amplitudes, and it shares the same features for both triblock copolymers. Furthermore, the asymmetry in

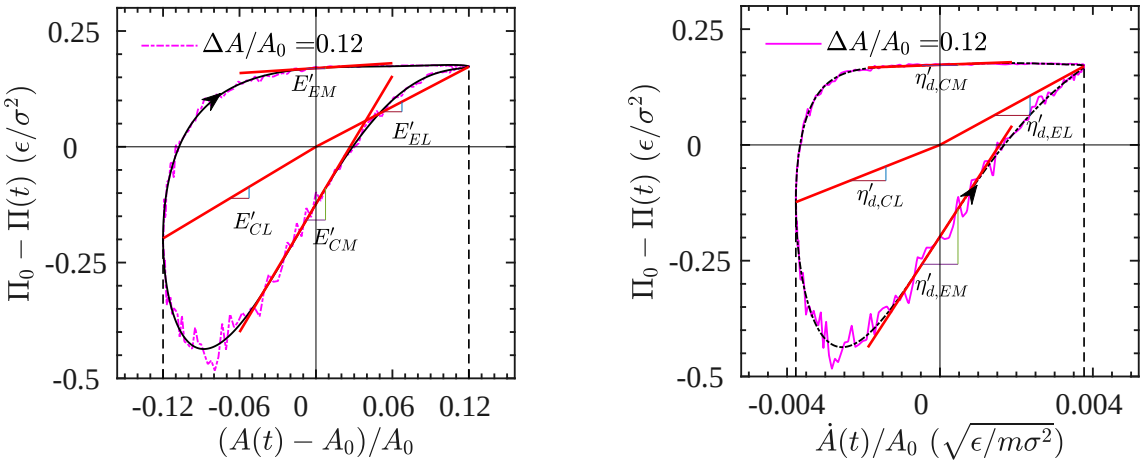

Figure 10: **(a)** A geometrical description of minimum- and large-strain dynamic dilatational moduli in extension (E'_{EM}, E'_{EL}), and compression (E'_{CM}, E'_{CL}) as presented in an elastic Lissajous plot. **(b)** Geometrically motivated dynamic minimum- and large-rate dilatational viscosities in extension ($\eta'_{d,\mathrm{EM}}$, $\eta'_{d,\mathrm{EL}}$), and compression ($\eta'_{d,\mathrm{CM}}$, $\eta'_{d,\mathrm{CL}}$) as presented in a viscous Lissajous plot. The signal depicted here corresponds to an interfacial film of $\mathrm{H_{21}T_8H_{21}}$ at a surface concentration of $\Gamma = 0.0278\,\sigma^{-2}$ deformed with a frequency of $f = 0.005\sqrt{\epsilon/m\sigma^2}$. Only the first four harmonics of the raw signal (black lines) are used to evaluate the moduli and viscosities (the slope of the red lines).

the shape of S_{E} compared to S_{C} is indicative of the fact that the interfacial microstructure changes also asymmetrically in extension with respect to compression. While the overal response shows strain softening at large strain amplitudes, as revealed by amplitude sweeps (Fig. 7), this graphical analysis results in a paradoxical conclusion implying that the response is strain hardening in extension, a paradox which was recently observed and discussed in 3D LAOS[60] and later in LAOD,[18] and is attributed to the use of tangent moduli in these graphical analyses. However, consistent with recent experimental results,[18] a nonparadoxical behavior is observed in the strain-rate thickening factors (T_{E}, T_{C}) as indicated in Fig. 11b. More specifically, the viscous response is linear in small strain rates $T \approx 0$, strain rate-thinning in large extension rates ($T_{\mathrm{E}} < 0$), and strain rate-thickening in large compression rates ($T_{\mathrm{C}} > 0$). While Lissajous plots and nonlinearity indices provide valuable physical insights into the possible structural changes as a result of large deformations (rates), we complement these observations by looking at the interfacial microstructure in the deformed state, and compare it with the surface rheology data, in the next section.

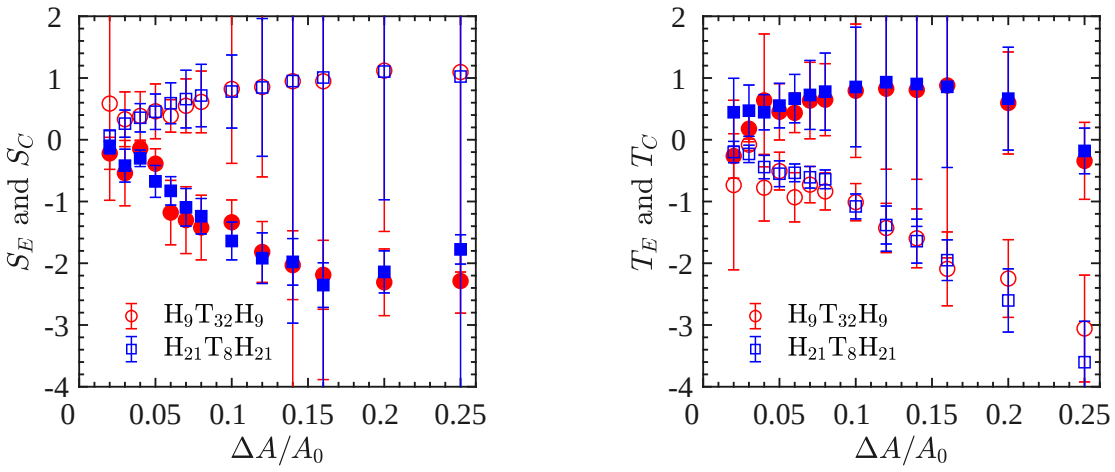

(a) (b)

Figure 11: Data obtained upon varying the imposed oscillatory strain amplitude. **(a)** Strain-hardening indices in extension S_{E} (open symbols) and compression S_{C} (close symbols) for $H_{21}T_8H_{21}$ (squares) at $\Gamma = 0.0384\sigma^{-2}$ and $H_9T_{32}H_9$ (circles) at $\Gamma = 0.0446\sigma^{-2}$. **(b)** Strain rate-thickening indices in extension T_{E} and compression T_{C} for the same data. These intracycle nonlinearity measures correspond to the Lissajous plots presented in Fig. 9 and the amplitude sweeps in Fig. 7. For $H_{21}T_8H_{21}$ triblock copolymer films at $\Gamma = 0.0278\,\sigma^{-2}$, the Lissajous plots and corresponding S- and T-factors are calculated and presented in the Supplementary Information section S3.

Structure-rheology relationship

In this section, we characterize the interfacial microstructure in the deformed state and try to establish its link with the surface rheology data.

As revealed by our equilibrium MD simulations, normal and parallel components of radius of gyration, $R_g^{\perp}$ and $R_g^{\parallel}$, describe the interface at the molecular level very well. Here we capture the interfacial microstructure through calculation of $R_g^{\perp}(t)$ and $R_g^{\parallel}(t)$ as a function of applied deformation as described in Eq. 9. The parametric plots of $R_g^{\perp}$ and $R_g^{\parallel}$ corresponding to the Lissajous plots in Fig. 9 for interfacial films of $H_{21}T_8H_{21}$ at $\Gamma = 0.0384\sigma^{-2}$ and $H_9T_{32}H_9$ at $\Gamma = 0.0446\sigma^{-2}$ are presented in Fig. 12. These figures clearly show that these structural variables also vary in an oscillatory manner, and have a certain phase shift with respect to the deformation field, as revealed by the nonzero width of these parametric curves. Furthermore, at relatively small strain amplitudes the shape is close to an ellipse, an indication of the absence of higher harmonics, as

in the stress response in the linear regime. Similar to the Lissajous plots (Fig. 9), upon increasing the strain amplitude, the graphs become asymmetric, which translates into different structural changes in compression compared to extension. Moreover, the signals corresponding to $R_g^{\parallel}$ and $R_g^{\perp}$ vary completely out of phase. More specifically, in the initial stage of compression (upper half portions of the curves in Fig. 12a and 12c and lower half portions of the curves in Fig. 12b and 12d) a flattening in both signals is observed, which means that only intermolecular distances decrease upon compression and the internal structure of chains is not deformed. It is then followed by an increase (decrease) in $R_g^{\perp}$ ($R_g^{\parallel}$) until the end of compression stroke, indicating that while chains shrink laterally, they get extended toward the bulk phase upon compression. In the extension stroke (lower half portions of the curves in Figs. 12a and 12c and upper half portions of the curves in Figs. 12b and 12d) $R_g^{\perp}$ ($R_g^{\parallel}$) decrease (increases) rather monotonically which means that the chains retract toward the interface, and at the same time they expand laterally. A reason for this asymmetric behavior is that in the compression stage the structural changes are imposed by the barriers' motion, while in the extension stroke the chains are free to follow the barriers through their natural in-plane relaxation. A comparison between interfacial films of $H_{21}T_8H_{21}$ (Figs. 12b and 12a) and $H_9T_{32}H_9$ (Figs. 12d and 12c) reveals that the microstructural changes of these polymeric films share the same features, despite of them having a different degree of hydrophobicity. We note here that S- and T-factors, shown in Figs. 11a and 11b, also show the same trend for both $H_{21}T_8H_{21}$ and $H_9T_{32}H_9$ triblock copolymers, further validating that these nonlinearity indices are closely related to the interfacial microstructural changes.[49]

In order to quantify these structural changes as a result of applied deformation, similar to the first harmonic analysis of the stress signal (Eq. 13), the amplitude of the parallel radius of gyration $\Delta R_g^{\parallel}$ is obtained through fitting the simulation data to

$$R_g^{\parallel}(t) - \langle R_g^{\parallel} \rangle = \Delta R_g^{\parallel} \sin(\omega t + \delta_2), \tag{17}$$

where δ_2 is the phase shift of the structure signal with respect to the applied deformation (Eq. 9).

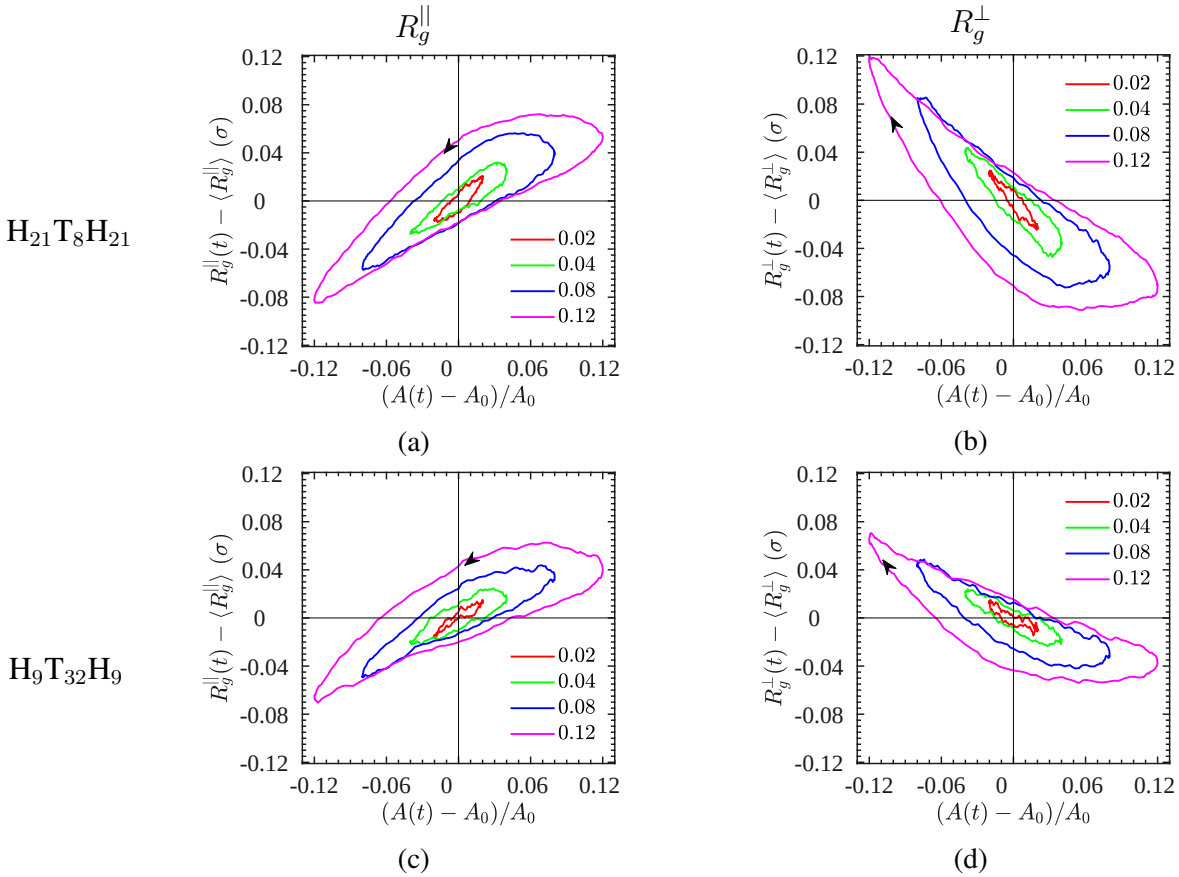

Figure 12: Parametric plots of normal $R_g^{\perp}$ and parallel $R_g^{||}$ components of radius of gyration corresponding to the LOAD data shown in Fig. 7 for $H_{21}T_8H_{21}$ and $H_9T_{32}H_9$ evaluated at different strain amplitudes shown by different colors in the graphs. The top row shows the data for $H_{21}T_8H_{21}$ interfacial films at $\Gamma = 0.0384\,\sigma^{-2}$ and the bottom row for $H_9T_{32}H_9$ at $\Gamma = 0.0446\,\sigma^{-2}$. Corresponding plots for interfacial films of $H_{21}T_8H_{21}$ at another surface concentration $\Gamma = 0.0278\,\sigma^{-2}$ are shown in the Supplementary Information section S4.

The results of $\Delta R_g^{||}$ are presented in Fig. 13a for different surface concentrations of $H_{21}T_8H_{21}$ (circles and diamonds) and $H_9T_{32}H_9$ (squares) as a function of strain amplitude. The amplitude of corresponding stress signals $\Delta\Pi$ used to calculate first harmonic moduli (obtained from Eq. 13) are also shown in Fig. 13b. A comparison between these two figures indicates that $\Delta R_g^{||}$ and $\Delta\Pi$ follow a similar trend; they both grow linearly with $\Delta A/A_0$ at relatively small strain amplitudes (linear regime) which is then followed by a sub-linear behavior (softening region).

That both quantities follow a similar trend can be observed more clearly in Fig. 14, where a parametric plot of $\Delta\Pi(\Delta A/A_0)$ as a function of $\Delta R_g^{||}(\Delta A/A_0)$ is depicted. It clearly shows

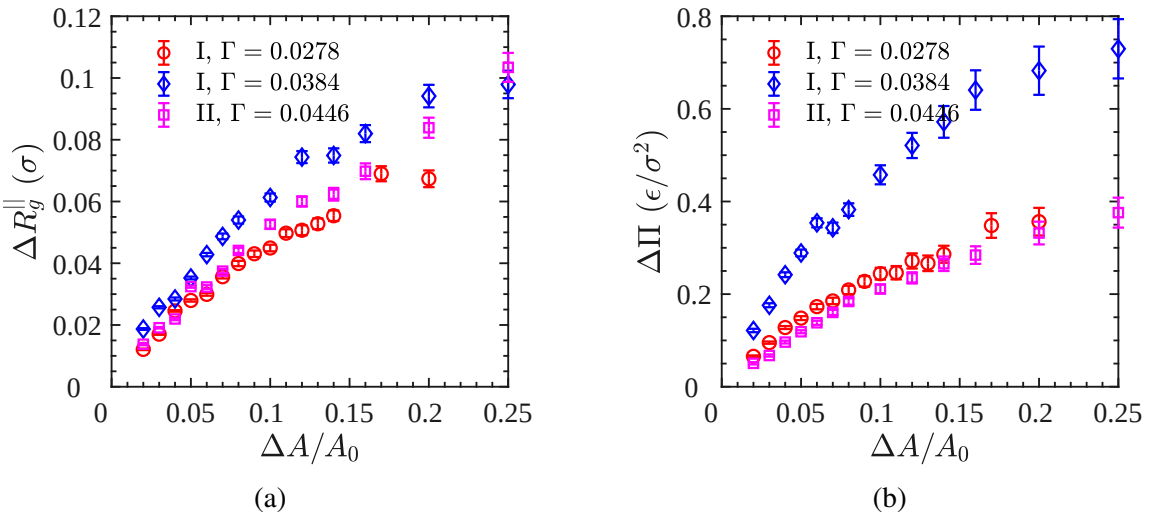

(a) (b)

Figure 13: First harmonic analysis of parallel radius of gyration **(a)** and surface stress **(b)** signals as a function of the imposed oscillatory strain amplitude for $H_{21}T_8H_{21}$ at surface concentrations of $\Gamma = 0.0278\,\sigma^{-2}$ (circles) and $0.0384\,\sigma^{-2}$ (diamonds), and $H_9T_{32}H_9$ at $\Gamma = 0.0446\sigma^{-2}$ (squares). The data presented here correspond to the raw structure and stress signals presented in Fig. 12 and 9, respectively.

the link between interfacial rheology ($\Delta\Pi$) and microstructure ($\Delta R_g^{\parallel}$) of triblock copolymer films studied in this research. It is noteworthy that while dilatational strain amplitude grows up to 25%, the relative changes in $\Delta R_g^{\parallel}$ only increase at most by $\Delta R_g^{\parallel}/R_g^{\parallel} \approx 0.1/3.1 \approx 3\%$ ($R_g^{\parallel}$ obtained from Fig. 4b). While at large deformations the first harmonics of the stress and structure signals vary nonlinearly with strain amplitude, we find a linear relationship between them (dash-dotted lines in Fig. 14 which holds over the relatively small range of $\Delta R_g^{\parallel}/R_g^{\parallel}$ values explored here. The slope of the lines in Fig. 14 indicate the strength of the viscoelastic films against changes in the microstructure. Interfacial films of $H_{21}T_8H_{21}$ respond stronger to microstructural changes than $H_9T_{32}H_9$ even at relatively smaller surface concentrations, in accordance with the results of amplitude sweeps shown in Fig. 7.

Conclusion

Surface layers of model amphiphilic triblock copolymers at a liquid–vapor interface were studied by means of MD simulations and compared qualitatively with the results of recent experiments.

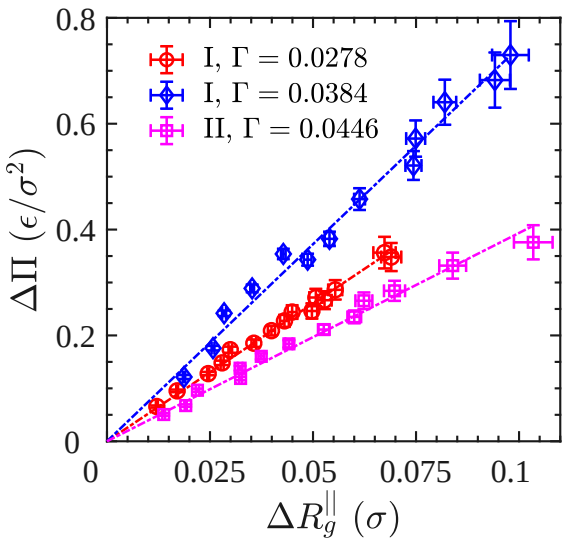

Figure 14: Surface structure–rheology relationship in terms of the parametric plot of surface stress $\Delta\Pi(\Delta A/A_0)$ as a function of surface structure $\Delta R_g^{\parallel}(\Delta A/A_0)$ amplitude for $H_{21}T_8H_{21}$ at surface concentrations of $\Gamma = 0.0278\,\sigma^{-2}$ (circles) and $0.0384\,\sigma^{-2}$ (diamonds), and $H_9T_{32}H_9$ at $\Gamma = 0.0446\sigma^{-2}$ (squares). Dash-dotted lines indicate the best linear fit passing through the origin.

The effect of hydrophilic/hydrophobic block length ratio and surface concentration on both equilibrium and dynamic properties of these interfaces were studied in detail. The simulations revealed that triblock copolymers with a larger hydrophilic/hydrophobic block length ratio take a conformation with a larger radius of gyration, impart a higher surface pressure to the interface, and show a slower chain relaxation at a given surface concentration.

Inspired by Langmuir trough experiments, a new method involving semipermeable barriers (SPB) was proposed and successfully tested which captures dynamic properties of the oscillating, dilated or sheared interface using NEMD simulations at constant number of particles. Surface dilatational rheology simulations in the linear regime revealed that more hydrophilic chains form a stronger viscoelastic film even at relatively smaller surface concentrations. Furthermore, a different power law behavior than that of the Maxwell model at small frequency domain for both dilatational moduli was observed, which suggests that generalization of bulk rheology models to interfacial rheology does not work here possibly due to the coupling to the bulk.[15]

LAOD tests were performed and the corresponding Lissajous plots were analyzed geometrically to quantify intracycle elastic and viscous nonlinearities by means of strain-stiffening and

strain rate-thickening indices in extension and compression. In accordance with recent experiments[18,60] a strain hardening/strain softening paradox was also observed here. We found that these nonlinearity indices are closely related to interfacial microstructural changes, namely changes in the normal and parallel radii of gyration with respect to the interface plane. The interfacial microstructure in the deformed state at different strain amplitudes was captured and a first harmonic analysis of the surface stress and structure signal suggested a linear relationship between these two variables. Therefore, a surface structure-rheology relationship was obtained for interfacial films of model triblock copolymers in this research.

Here we have chosen a CG model system consisting of relatively short semiflexible triblock copolymers, whose relaxation time does not pose a major computational challenge. Simulations for longer chains with more conformational freedom could be performed to investigate possible entanglement effects on both equilibrium and dynamic interfacial properties. The schemes presented here for both surface dilatational and shear rheology simulations can be extended straightforwardly towards other surface active components at fluid-fluid interfaces and thus provide a basis to develop and motivate constitutive models which link the surface rheology to the interfacial microstructure.[1,49] They help to interpret experimental data obtained from surface rheology and microstructure characterization experiments and might ultimately be used to tune the properties of multiphase systems containing complex interfaces.

Acknowledgment

This research was supported by the Swiss National Science Foundation through Grants No. 200021_156106 and 200021L_185052.

Supporting Information

Local density profiles of H- and T blocks across the interface; surface tension time series and its autocorrelation; in-plane velocity profiles in the deformed state; Lissajous plots, nonlinearity

indices, and the surface structure for $H_{21}T_8H_{21}$ at $\Gamma = 0.0278\,\sigma^{-2}$; description of the surface shear rheology

References

(1) Sagis, L. M. C. Dynamic properties of interfaces in soft matter: Experiments and theory. *Rev. Mod. Phys.* **2011**, *83*, 1367–1403, DOI: 10.1103/RevModPhys.83.1367.

(2) Hilles, H.; Monroy, F.; Bonales, L. J.; Ortega, F.; Rubio, R. G. Fourier-transform rheology of polymer Langmuir monolayers: Analysis of the non-linear and plastic behaviors. *Adv. Colloid Interf. Sci.* **2006**, *122*, 67–77, DOI: 10.1016/j.cis.2006.06.013.

(3) Hilles, H.; Maestro, A.; Monroy, F.; Ortega, F.; Rubio, R. G.; Velarde, M. G. Polymer monolayers with a small viscoelastic linear regime: Equilibrium and rheology of poly(octadecyl acrylate) and poly(vinyl stearate). *J. Chem. Phys.* **2007**, *126*, 124904, DOI: 10.1063/1.2714514.

(4) George, S.; Champagne-Hartley, R.; Deeter, G.; Campbell, D.; Reck, B.; Urban, D.; Cunningham, M. Amphiphilic Block Copolymers as Stabilizers in Emulsion Polymerization: Effects of the Stabilizing Block Molecular Weight Dispersity on Stabilization Performance. *Macromolecules* **2015**, *48*, 8913–8920, DOI: 10.1021/acs.macromol.5b01853.

(5) Fauré, M.; Bassereau, P.; Carignano, M.; Szleifer, I.; Gallot, Y.; Andelman, D. Monolayers of diblock copolymer at the air-water interface: the attractive monomer-surface case. *Eur. Phys. J. B* **1998**, *3*, 365–375, DOI: 10.1007/s100510050324.

(6) Hilles, H. M.; Sferrazza, M.; Monroy, F.; Ortega, F.; Rubio, R. G. Equilibrium and dynamics of Langmuir monolayers when the interface is a selective solvent: Polystyrene-b-poly(t-butyl acrylate) block copolymers. *J. Chem. Phys.* **2006**, *125*, 074706, DOI: 10.1063/1.2238868.

(7) Fauré, M. C.; Bassereau, P.; Lee, L. T.; Menelle, A.; Lheveder, C. Phase Transitions in Monolayers of PS-PEO Copolymer at the Air-Water Interface. *Macromolecules* **1999**, *32*, 8538–8550, DOI: 10.1021/ma9900840.

(8) Devereaux, C. A.; Baker, S. M. Surface features in Langmuir-Blodgett monolayers of predominantly hydrophobic poly(styrene)-poly(ethylene oxide) diblock copolymer. *Macromolecules* **2002**, *35*, 1921–1927, DOI: 10.1021/ma011319m.

(9) Hosoi, A. E.; Kogan, D.; Devereaux, C. E.; Bernoff, A. J.; Baker, S. M. Two-dimensional self-assembly in diblock copolymers. *Phys. Rev. Lett.* **2005**, *95*, 037801, DOI: 10.1103/PhysRevLett.95.037801.

(10) Seo, Y.; Im, J.-H.; Lee, J.-S.; Kim, J.-H. Aggregation Behaviors of a Polystyrene-b-poly(methyl methacrylate) Diblock Copolymer at the Air/Water Interface. *Macromolecules* **2001**, *34*, 4842–4851, DOI: 10.1021/ma002119y.

(11) Meszaros, M.; Eisenberg, A.; Lennox, R. B. Block copolymer self-assembly in two dimensions: nanoscale emulsions and foams. *Faraday Discuss.* **1994**, *98*, 283, DOI: 10.1039/fd9949800283.

(12) Li, S.; Hanley, S.; Khan, I.; Varshney, S. K.; Eisenberg, A.; Lennox, R. B. Surface micelle formation at the air/water interface from nonionic diblock copolymers. *Langmuir* **1993**, *9*, 2243–2246, DOI: 10.1021/la00032a057.

(13) Cox, J. K.; Yu, K.; Eisenberg, A.; Lennox, R. B. Compression of polystyrene–poly(ethylene oxide) surface aggregates at the air/water interface. *Phys. Chem. Chem. Phys.* **1999**, *1*, 4417–4421, DOI: 10.1039/a905008f.

(14) Bijsterbosch, H. D.; de Haan, V. O.; de Graaf, A. W.; Mellema, M.; Leermakers, F. A. M.; Stuart, M. A. C.; van Well, A. A. Tethered Adsorbing Chains: Neutron Reflectivity and Surface Pressure of Spread Diblock Copolymer Monolayers. *Langmuir* **1995**, *11*, 4467–4473, DOI: 10.1021/la00011a047.

(15) Sagis, L. M. C.; Liu, B.; Li, Y.; Essers, J.; Yang, J.; Moghimikheirabadi, A.; Hinderink, E.; Berton-Carabin, C.; Schroen, K. Dynamic heterogeneity in complex interfaces of soft interface-dominated materials. *Sci. Rep.* **2019**, *9*, 2938, DOI: 10.1038/s41598-019-39761-7.

(16) Alexandridis, P.; Holzwarth, J. F.; Hatton, T. A. Micellization of Poly(ethylene oxide)-Poly(propylene oxide)-Poly(ethylene oxide) Triblock Copolymers in Aqueous Solutions: Thermodynamics of Copolymer Association. *Macromolecules* **1994**, *27*, 2414–2425, DOI: 10.1021/ma00087a009.

(17) Alexandridis, P.; Lindman, B. *Amphiphilic Block Copolymers: Self-Assembly and Applications*; Elsevier: Amsterdam, 2000.

(18) Moghimikheirabadi, A.; Fischer, P.; Kröger, M.; Sagis, L. M. C. Relaxation Behavior and Nonlinear Surface Rheology of PEO–PPO–PEO Triblock Copolymers at the Air–Water Interface. *Langmuir* **2019**, *35*, 14388–14396.

(19) Noskov, B. A.; Lin, S.-Y.; Loglio, G.; Rubio, R. G.; Miller, R. Dilational Viscoelasticity of PEO-PPO-PEO Triblock Copolymer Films at the Air-Water Interface in the Range of High Surface Pressures. *Langmuir* **2006**, *22*, 2647–2652, DOI: 10.1021/la052662d.

(20) Muñoz, M. G.; Monroy, F.; Ortega, F.; Rubio, R. G.; Langevin, D. Monolayers of Symmetric Triblock Copolymers at the Air-Water Interface. 1. Equilibrium Properties. *Langmuir* **2000**, *16*, 1083–1093, DOI: 10.1021/la990142a.

(21) Blomqvist, B. R.; Wärnheim, T.; Claesson, P. M. Surface Rheology of PEO-PPO-PEO Triblock Copolymers at the Air-Water Interface: Comparison of Spread and Adsorbed Layers. *Langmuir* **2005**, *21*, 6373–6384, DOI: 10.1021/la0467584.

(22) Sedev, R.; Steitz, R.; Findenegg, G. The structure of PEO–PPO–PEO triblock copolymers at the water/air interface. *Physica B* **2002**, *315*, 267–272, DOI: 10.1016/s0921-4526(02)00513-6.

(23) Vieira, J. B.; Li, Z. X.; Thomas, R. K.; Penfold, J. Structure of triblock copolymers of ethylene oxide and propylene oxide at the air/water interface determined by neutron Reflection. *J. Phys. Chem. B* **2002**, *106*, 10641–10648, DOI: 10.1021/jp013851h.

(24) Hurcom, J.; Paul, A.; Heenan, R. K.; Davies, A.; Woodman, N.; Schweins, R.; Griffiths, P. C. The interfacial structure of polymeric surfactant stabilised air-in-water foams. *Soft Matter* **2014**, *10*, 3003–3008, DOI: 10.1039/C3SM52877D.

(25) Kim, C.; Yu, H. Surface rheology of monolayers of triblock copolymers of PEO and PPO: Surface light scattering studies at the air/water interface. *Langmuir* **2003**, *19*, 4460–4464, DOI: 10.1021/la034092s.

(26) Noskov, B. A. Dynamic elasticity of triblock copolymer of poly(ethylene oxide) and poly(propylene oxide) on a water surface. *Colloid J.* **2006**, *68*, 588–596, DOI: 10.1134/s1061933x06050103.

(27) Hansen, F. K. Surface dilatational elasticity of poly(oxy ethylene)-based surfactants by oscillation and relaxation measurements of sessile bubbles. *Langmuir* **2008**, *24*, 189–197, DOI: 10.1021/la7024582.

(28) Chen, C.; Even, M. A.; Chen, Z. Detecting Molecular-Level Chemical Structure and Group Orientation of Amphiphilic PEO-PPO-PEO Copolymers at Solution/Air and Solid/Solution Interfaces by SFG Vibrational Spectroscopy. *Macromolecules* **2003**, *36*, 4478–4484.

(29) Alexandridis, P.; Hatton, T. A. Poly(ethylene oxide)-poly(propylene oxide)-poly(ethylene oxide) block copolymer surfactants in aqueous solutions and at interfaces: thermodynamics, structure, dynamics, and modeling. *Colloids Surf., A* **1995**, *96*, 1–46.

(30) Nawaz, S.; Redhead, M.; Mantovani, G.; Alexander, C.; Bosquillon, C.; Carbone, P. Interactions of PEO–PPO–PEO block copolymers with lipid membranes: a computational and experimental study linking membrane lysis with polymer structure. *Soft Matter* **2012**, *8*, 6744.

(31) Nawaz, S.; Carbone, P. Coarse-Graining Poly(ethylene oxide)–Poly(propylene oxide)–Poly(ethylene oxide) (PEO–PPO–PEO) Block Copolymers Using the MARTINI Force Field. *J. Phys. Chem. B* **2014**, *118*, 1648–1659.

(32) Kröger, M.; Loose, W.; Hess, S. Rheology and structural changes of polymer melts via nonequilibrium molecular dynamics. *J. Rheol.* **1993**, *37*, 1057–1079, DOI: 10.1122/1.550409.

(33) Kröger, M.; Luap, C.; Muller, R. Polymer melts under uniaxial elongational flow: Stress-optical behavior from experiments and nonequilibrium molecular dynamics computer simulations. *Macromolecules* **1997**, *30*, 526–539, DOI: 10.1021/ma960317c.

(34) Aust, C.; Kröger, M.; Hess, S. Structure and dynamics of dilute polymer solutions under shear flow via nonequilibrium molecular dynamics. *Macromolecules* **1999**, *32*, 5660–5672, DOI: 10.1021/ma981683u.

(35) Cifre, J. G. H.; Hess, S.; Kröger, M. Linear viscoelastic behavior of unentangled polymer melts via non-equilibrium molecular dynamics. *Macromol. Theory Simul.* **2004**, *13*, 748–753, DOI: 10.1002/mats.200400021.

(36) Zheng, Z.; Liu, H.; Shen, J.; Liu, J.; Wu, Y.; Zhang, L. Tailoring the static and dynamic mechanical properties of tri-block copolymers through molecular dynamics simulation. *Polymers* **2016**, *8*, 335, DOI: 10.3390/polym8090335.

(37) Moghimikheirabadi, A.; Sagis, L. M.; Ilg, P. Effective interaction potentials for model amphiphilic surfactants adsorbed at fluid–fluid interfaces. *Phys. Chem. Chem. Phys.* **2018**, *20*, 16238–16246, DOI: 10.1039/c8cp01632a.

(38) Moghimikheirabadi, A.; Sagis, L. M. C.; Kröger, M.; Ilg, P. Gas–liquid phase equilibrium of a model Langmuir monolayer captured by a multiscale approach. *Phys. Chem. Chem. Phys.* **2019**, *21*, 2295–2306, DOI: 10.1039/c8cp05447a.

(39) Brooks, C. F.; Fuller, G. G.; Frank, C. W.; Robertson, C. R. An interfacial stress rheometer to study rheological transitions in monolayers at the air-water interface. *Langmuir* **1999**, *15*, 2450–2459, DOI: 10.1021/la980465r.

(40) Verwijlen, T.; Moldenaers, P.; Stone, H. A.; Vermant, J. Study of the flow field in the magnetic rod interfacial stress rheometer. *Langmuir* **2011**, *27*, 9345–9358, DOI: 10.1021/la201109u.

(41) Wijmans, C. M.; Dickinson, E. Simulation of interfacial shear and dilatational rheology of an adsorbed protein monolayer modeled as a network of spherical particles. *Langmuir* **1998**, *14*, 7278–7286, DOI: 10.1021/la980687p.

(42) Pugnaloni, L. A.; Ettelaie, R.; Dickinson, E. Computer Simulation of the Microstructure of a Nanoparticle Monolayer Formed under Interfacial Compression. *Langmuir* **2004**, *20*, 6096–6099, DOI: 10.1021/la049213i.

(43) Pugnaloni, L. A.; Ettelaie, R.; Dickinson, E. Brownian dynamics simulation of adsorbed layers of interacting particles subjected to large extensional deformation. *J. Colloid Interf. Sci.* **2005**, *287*, 401–414, DOI: 10.1016/j.jcis.2005.02.024.

(44) Luo, A. M.; Sagis, L. M. C.; Öttinger, H. C.; Michele, C. D.; Ilg, P. Modelling the rheology of anisotropic particles adsorbed on a two-dimensional fluid interface. *Soft Matter* **2015**, *11*, 4383–4395, DOI: 10.1039/c5sm00372e.

(45) Todd, B.; Daivis, P. *Nonequilibrium Molecular Dynamics: Theory, Algorithms and Applications*; Cambridge University Press, 2017.

(46) Schlossman, M. L.; Tikhonov, A. M. Molecular ordering and phase behavior of surfactants at water-oil interfaces as probed by X-ray surface scattering. *Annu. Rev. Phys. Chem.* **2008**, *59*, 153–177, DOI: 10.1146/annurev.physchem.59.032607.093822.

(47) Kremer, K.; Grest, G. S. Dynamics of entangled linear polymer melts - A molecular dynamics simulation. *J. Chem. Phys.* **1990**, *92*, 5057–5086.

(48) Ewoldt, R. H.; Hosoi, A. E.; McKinley, G. H. New measures for characterizing nonlinear viscoelasticity in large amplitude oscillatory shear. *J. Rheol.* **2008**, *52*, 1427–1458, DOI: 10.1122/1.2970095.

(49) Sagis, L. M.; Fischer, P. Nonlinear rheology of complex fluid–fluid interfaces. *Curr. Opin. Colloid Interf. Sci.* **2014**, *19*, 520–529, DOI: 10.1016/j.cocis.2014.09.003.

(50) Plimpton, S. Fast parallel algorithms for short-range molecular dynamics. *J. Comput. Phys.* **1995**, *117*, 1 – 19, DOI: http://dx.doi.org/10.1006/jcph.1995.1039.

(51) Walton, J.; Tildesley, D.; Rowlinson, J.; Henderson, J. The pressure tensor at the planar surface of a liquid. *Mol. Phys.* **1983**, *48*, 1357–1368, DOI: 10.1080/00268978300100971.

(52) Trokhymchuk, A.; Alejandre, J. Computer simulations of liquid/vapor interface in Lennard-Jones fluids: Some questions and answers. *J. Chem. Phys.* **1999**, *111*, 8510–8523.

(53) Heyes, D. M. The Lennard-Jones fluid in the liquid-vapour critical region. *CMST* **2015**, *21*, 169–179.

(54) Kozuch, D.; Zhang, W.; Milner, S. Predicting the Flory-Huggins χ parameter for polymers with stiffness mismatch from molecular dynamics simulations. *Polymers* **2016**, *8*, 241.

(55) Rowlinson, J.; Widom, B. *Molecular Theory of Capillarity*; Dover books on chemistry; Dover Publications, 2002.

(56) Lee, W. B.; Kremer, K. Entangled polymer melts: Relation between plateau modulus and stress autocorrelation function. *Macromolecules* **2009**, *42*, 6270–6276.

(57) Venerus, D. C.; Öttinger, H. C. *A Modern Course in Transport Phenomena*; Cambridge University Press, 2018; Chapter 12.

(58) Luap, C.; Goedel, W. A. Linear viscoelastic behavior of end-tethered polymer monolayers at the air/water interface. *Macromolecules* **2001**, *34*, 1343–1351, DOI: 10.1021/ma991485i.

(59) Lucassen, J.; Tempel, M. V. D. Dynamic measurements of dilational properties of a liquid interface. *Chem. Eng. Sci.* **1972**, *27*, 1283–1291, DOI: 10.1016/0009-2509(72)80104-0.

(60) Mermet-Guyennet, M. R. B.; Gianfelice de Castro, J.; Habibi, M.; Martzel, N.; Denn, M. M.; Bonn, D. LAOS: The strain softening/strain hardening paradox. *J. Rheol.* **2015**, 21–32, DOI: 10.1122/1.4902000.

Graphical TOC Entry